

Department of Physics and Astronomy

University of Heidelberg

Master thesis

in Physics

submitted by

Sarah Philips

born in Fürth

2023

Characterizing a High-Resolution Imaging System for the Dysprosium Experiment

This Master thesis has been carried out by Sarah Philips
at the
Ruprecht Karl University of Heidelberg
under the supervision of
Prof. Dr. Lauriane Chomaz

Abstract

The Dysprosium Lab of the Quantum Fluids group at the University Heidelberg explores a dipolar Bose-Einstein Condensate of dysprosium, the most magnetic atom. Ultracold quantum gases, with their tunable interactions, are an ideal platform to observe quantum phenomena, while the dipolar regime enables additional degrees of control. In this thesis, the characterization of a high-resolution imaging system is presented. Using a test setup, the optical assembly was prepared and the properties of the custom-designed microscope objective with a numerical aperture of 0.6 were investigated carefully. To check its overall performance, a nanopore target was used together with the four different wavelengths of interest for the experiment. Theoretical thoughts as well as experimental results of the measurements are discussed. The minimal observed resolution was 483 nm at a wavelength of 405 nm. Over the whole field of view, the average resolution was $(0.60 \pm 0.13) \mu\text{m}$ at the same wavelength. Additionally, properties like depth of field, tilt behavior, and chromatic focal shift were observed and an alignment procedure was tested. The setup was transferred into the main experiment and will be used to image the atomic cloud.

Kurzfassung

Im Dysprosium Labor der Quantum Fluids Gruppe an der Universität Heidelberg wird dipolare Bose-Einstein-Kondensation von Dysprosium-Atomen in einem neuartigen experimentellen Aufbau erforscht. Ultrakalte Quantengase sind eine ideale Plattform, um Quantenphänomene zu beobachten, da sie steuerbare Wechselwirkungen ermöglichen, während das dipolare Regime weitere Freiheitsgrade mit sich bringt. In dieser Arbeit wird die Charakterisierung eines hochauflösenden Abbildungssystems präsentiert. Mit einem Testaufbau wurde das optische Equipment geprüft und die Eigenschaften des individuell gestalteten Mikroskopobjektivs sorgfältig bestimmt. Um dessen generelle Leistung zu testen, wurden Nanoporen als Referenz gemeinsam mit vier verschiedenen Wellenlängen verwendet, die für das Experiment von Interesse sind. Die theoretischen Überlegungen sowie die experimentellen Ergebnisse der Messungen werden diskutiert. Die minimal gemessene Auflösung war 483 nm bei einer Wellenlänge von 405 nm. Über das gesamte Sichtfeld ist die durchschnittliche Auflösung $(0.60 \pm 0.13) \mu\text{m}$ bei derselben Wellenlänge. Zusätzlich wurden Eigenschaften wie die Tiefenschärfe, das Verhalten unter Neigungswinkel und die chromatische Fokalverschiebung gemessen und ein Justierungsschema getestet. Der Aufbau wurde in das Experiment transferiert und soll dort genutzt werden, um die Atomwolke mit hoher Auflösung abzubilden.

Contents

1	Introduction	1
2	The Dysprosium Experiment	3
2.1	Ultracold Quantum Gases	3
2.2	Properties of Dysprosium	4
2.3	Experimental Setup	7
2.4	Imaging Techniques	9
3	Theory of Imaging and Simulation Principle	13
3.1	Fourier Optics	13
3.2	Diffraction Limit	16
3.3	Aberrations	18
3.4	Principle of the Simulations of our Imaging Setup	21
4	Design of the Objective	25
4.1	Mechanical Design	25
4.2	Working Distance	26
4.3	Numerical aperture	27
4.4	Focal Length	27
4.5	Magnification	28
4.6	Back Focal Plane	28
4.7	Resolution	29
4.8	Depth of Field	30
4.9	Field of View	31
4.10	Chromatic focal shift	31
4.11	Transmission	32
5	Experimental Realisation	35
5.1	Test Setup Design	36
5.2	Alignment	38
5.3	Measurements with a commercial Objective	40
5.4	Characterization of the custom-designed Objective	43
5.4.1	Magnification	43
5.4.2	Back Focal Plane	44
5.4.3	Resolution	45
5.4.4	Depth of Field	47
5.4.5	Field of View	48
5.4.6	Aberrations and Tilt	50

5.4.7	Chromatic Focal Shift	51
5.4.8	Transmission	52
5.4.9	Imaging Setup including a Dichroic Mirror	53
6	Implementation	56
6.1	Final Assembly	56
6.2	Magnification	58
7	Summary and Outlook	60
A	Appendix	62
A.1	Technical Drawings	62
A.2	Pictures	68
B	Bibliography	70

1 Introduction

In 2001, Nobel laureate in Physics Wolfgang Ketterle stated that "Bose-Einstein condensation is one of the most intriguing phenomena predicted by quantum statistical mechanics" [1]. The quest to create and study ultracold quantum gases has revolutionized our understanding of quantum mechanics and has led to breakthroughs in several different fields [2]. From simulating exotic condensed matter systems to probing new states of matter, ultracold quantum gases have opened up new possibilities in scientific research [3]. Moreover, they have enabled the development of advanced technologies, including ultra-precise atomic clocks [4], quantum simulators [5], and quantum computers [6]. One goal in the ultracold atom community is to gain local control and probing capability. An important tool are atom-light interactions, providing new methods for optical trapping and detection of neutral atoms as they enable strong control, optical manipulation, and high-resolution detection [7]. A particular strength is the number of detection methods that are available. By tailoring the detection process, specific scientific questions can be explored in the experiment. The images provide crucial information for investigating the properties of the atomic gas. One tool to achieve this is an imaging system including a microscope objective to probe the ultracold atomic cloud with high resolution. For now, this local control imaging has been little used in a setting with dipolar quantum gases while new physics have been observed in these systems. Due to the long-range and anisotropic dipole-dipole interactions competing with isotropic short-range contact interactions, new phenomena, such as quantum droplets and supersolids, were observed [8].

Outline: In this thesis, the characterization of a microscope objective for a high-resolution imaging system will be presented. This includes the description of a test setup and measurements for determining specific properties. The gained knowledge was used to implement the imaging system into the ultracold atom experiment with dysprosium at the Quantum Fluids group in September 2023.

Chapter 2 will introduce the field of ultracold quantum gases with a focus on Bose-

Einstein condensates. Since the here presented cold atom experiment is carried out with dysprosium, this element will be described by discussing its important properties. Subsequently, the experimental setup in its current status will be outlined in order to relate to the specific requirements that are set for the imaging system. Finally, the technique of absorption imaging, which is used for high-resolution imaging in our experiment, will be explained.

In Chapter 3, the theoretical concepts of imaging systems will be discussed for a better understanding of limitations and expectations for the experimental work. Thereby, the simulations of the optical performance and the underlying assumptions performed in the context of this thesis will be presented, as well as possibly occurring image errors.

A description of the custom-designed microscope objective, which is the basis of the high-resolution imaging setup, will be given in Chapter 4. The specific properties of this essential component will be defined in order to give a basis for the characterization measurements.

The test setup design will be sketched in Chapter 5, giving specifications of the individual parts. The measurements carried out within this test setup will be described, and by presenting the results, the performance of the objective will be characterized. The alignment procedure to ensure the best possible results will be described as well.

In Chapter 6, the implementation of the high-resolution imaging setup in the experiment will be outlined. The changes with respect to the test setup due to the mechanical constraints will be explained.

Chapter 7 will provide a summary of the thesis followed by an outlook on the future prospective of the experiment.

2 The Dysprosium Experiment

In the Dysprosium laboratory of the Quantum Fluids group at the University Heidelberg, a cold atom experiment has been constructed under the supervision of Lauriane Chomaz. This experiment aims to study quantum degenerate gases of dysprosium atoms in low dimensions. In this chapter, section 2.1 introduces the field of ultracold quantum gases, while section 2.2 describes the most important properties of dysprosium. Section 2.3 offers an overview of the experimental setup with its custom mechanical design. Finally, the technique of absorption imaging that will be used in the experiment to depict the atoms is explained in 2.4.

2.1 Ultracold Quantum Gases

Ultracold quantum gases are composed of atoms or molecules whose motion and interactions are precisely controlled and manipulated at the quantum level. They provide an ideal platform for exploring a wide range of quantum phenomena, such as Bose-Einstein condensation, fermionic superfluidity, quantum chemistry, and more.

One of the pioneering experiments in cold atom physics is the creation of a Bose-Einstein Condensate (BEC), where a dilute gas of bosonic atoms is cooled to extremely low temperatures close to absolute zero [2]. When the temperature falls below the critical temperature T_C in the Microkelvin regime, the system undergoes a phase transition. A macroscopic fraction of the bosons in the gas populates the lowest quantum state, forming a single quantum mechanical wave. Cooling techniques, such as laser cooling and evaporative cooling, are employed to lower the temperature of the bosons to the ultra-cold regime. In addition, the bosons must be trapped within a specific volume. Various methods, such as magnetic traps or optical traps are used for confinement. The density of particles in the trapping volume must be sufficiently high to achieve a large phase space density of the system to cross the phase transition. Since the background gas is very hot compared to the trapped atoms, any collision will lead to atom loss. By conducting experiments under a vacuum environment, the density of background gas

molecules is greatly reduced, minimizing collisions and preserving the ultracold state. The field has been a subject of great interest as it offers new insights into the behavior of matter at the quantum level.

After many efforts in the experimental techniques of laser trapping and cooling, the first Bose-Einstein-Condensations of rubidium and sodium were achieved in 1995. Both accomplishments were honored with the Nobel prize in 1997 [9, 10, 11], and in 2001 [12, 1], respectively. Another important step in the field of ultracold quantum gases was the realization of an optical dipole trap, allowing to hold atoms independent of their spin state and at various magnetic offset fields [13]. Confining the atoms in an optical lattice allows to observe quantum phase transitions like the bosonic superfluid to Mott transition [14]. When changing the dimensionality of the gas from 3D to lower dimensions, further effects can be observed, e.g. the Berezinsky–Kosterlitz–Thouless phase transition [15]. In the meantime, more elements were cooled to degeneracy, such as atomic hydrogen [16] and several alkali metals [17, 18, 19, 20]. Each of them comes with own challenges and prospects due to different physical properties. While the so far mentioned elements interact mainly through short-range contact interactions, atoms with large magnetic dipole moments offer the opportunity to use dipole-dipole interactions. This was first achieved with a dipolar BEC of chromium in 2005 [21]. Other elements followed, including dysprosium in 2011 [22]. Based on that, novel many-body quantum states were discovered, such as quantum droplets, droplet crystals, and supersolids [8]. Besides the preparation of the atomic cloud itself, precise detection techniques are an important part of these experiments to provide detailed insights into the processes. Common imaging methods allow to extract the momentum-space distribution of atomic clouds with time-of-flight measurements or to detect even individual atoms locally in two dimensions with quantum gas microscopes [7].

2.2 Properties of Dysprosium

Dysprosium is a chemical element that belongs to the lanthanide series of the periodic table and has an atomic number of 66. It was first discovered in 1886 by Paul Émile Lecoq de Boisbaudran, a French chemist. The name "dysprosium" is derived from the Greek word "dysprositos", which means "hard to get." This name reflects the difficulty in isolating this element from a holmium mineral in which it was found [23]. It was first isolated by the French chemist George Urbain in 1906. Dysprosium is a silvery metal

Isotope	^{160}Dy	^{161}Dy	^{162}Dy	^{163}Dy	^{164}Dy
Abundance [%]	2.3	18.9	25.5	24.9	28.3
Atomic mass [u]	159.93	160.93	161.93	162.93	163.93
Statistics	boson	fermion	boson	fermion	boson

Table 2.1: Abundances and properties of the most common stable dysprosium isotopes [23].

and is relatively stable in air at room temperature but can tarnish when exposed to moist air [24]. It is classified as a rare earth element due to its presence in the Earth's crust alongside other rare earth elements [25]. As many other lanthanide elements, Dy has a high melting temperature of 1412°C [26].

In nature, dysprosium has several stable isotopes, shown in Table 2.1. Four of them have relatively similar abundances, two of them follow bosonic statistics, and the other two follow fermionic statistics. In the here presented experiment, measurements are carried out with ^{164}Dy , the most abundant isotope.

With its 66 electrons, the ground state electronic contribution of dysprosium is

$$[1s^2 2s^2 2p^6 3s^2 3p^6 3d^{10} 4s^2 4p^6 4d^{10} 5s^2 5p^6]_{\text{Xe}} 4f^{10} 6s^2, \quad (2.1)$$

where the 54 electrons of the inner shell exhibit the structure of Xenon [26]. The closed outer 6s shell is filled by two electrons leading to convenient electronic transitions for laser cooling. In the 4f orbital, three electron pairs are formed and four electrons remain unpaired. This leads to an orbital angular momentum of $L=6$ and a total angular momentum of $J=8$ in the ground state, which can be written as 5I_8 in spectroscopic notation. The large electronic angular momentum is one of the most important characteristics of Dy, as it results in the largest magnetic moment among all elements in the periodic table, along with holmium. The magnetic moment of Dy is about 10 times larger than that of alkali atoms, hence it is a suitable quantum gas for studying dipolar interactions in a quantum system. This dipole-dipole interaction leads to long-range, anisotropic forces between dysprosium atoms, in contrast to the short-range, isotropic contact interactions.

Due to the complex level structure, the excitation spectrum of Dy is complex and offers many different decay channels. A small part of the level structure is shown in Figure 2.1. The broadest transition line at 421 nm between ground state $J=8$ and final state $J'=9$ has a decay rate of $\Gamma/2\pi = 32.2\text{ MHz}$. It can be used for the first cooling and

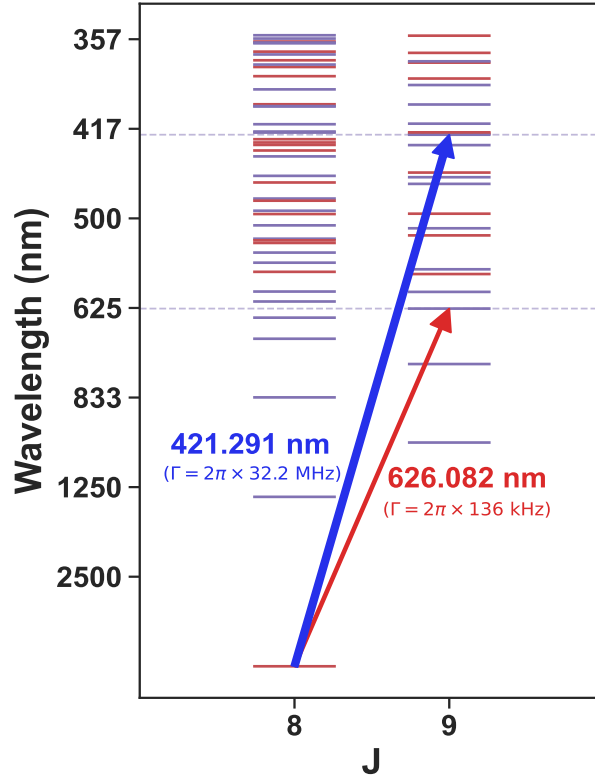


Figure 2.1: Energy level diagram of dysprosium for the levels of total electronic angular-momentum quantum number $J = 8$ and $J = 9$. The color of the energy states indicate their parity, where red relates to even and blue to odd parity. The used transitions are indicated with arrows, where the thickness of the arrows corresponds to their linewidths. Figure from [27].

deceleration processes [28]. Due to the large transition linewidth $\Delta\nu$, laser slowing and cooling are very efficient, allowing to capture atoms with large velocities. However, the minimal temperature achievable via standard laser cooling (Doppler temperature) is limited by the short lifetime of the excited state $1/\Gamma$ and calculates to $774 \mu\text{K}$. For cooling to lower temperatures, a narrow transition has to be chosen that comes with a smaller velocity at which the atoms can be captured. The 626 nm transition with its transition rate of $\Gamma/2\pi = 136 \text{ kHz}$ can be used, providing a lower Doppler temperature of $3.2 \mu\text{K}$ due to its narrow linewidth.

With its strong magnetic properties and complex energy levels, dysprosium is an interesting element for quantum physics experiments. It is notable for its numerous Feshbach resonances, which are effective tools for manipulating the short-range interactions of an ultracold gas [29]. The s-wave scattering length of a colliding pair of atoms exhibits a dependency on the magnetic field due to the presence of bound states

in different scattering channels, weakly coupled to the entrance collision channel. The energy of the closed channel can be shifted up and down relative to the energy of the entrance channel by applying a uniform magnetic field and tuning its strength [30]. When the scattering length is negative, the atoms are attracted to each other, while a positive scattering length indicates repulsion. The magnetic Feshbach resonances can be used to tune the relative strength of the short-range interactions and the long-range dipole-dipole interaction [31]. The complex level structure and coupling mechanisms of dysprosium give rise to a high density of narrow Feshbach resonances. This can be exploited to investigate different interaction regimes leading to exotic quantum states like dipolar quantum droplets and quantum ferrofluids [8]. These states exhibit unusual properties that are not observed in classical systems and provide valuable insights into fundamental quantum physics.

2.3 Experimental Setup

In the Dysprosium Lab in Heidelberg, we are building a new-generation experiment to cool and trap dysprosium atoms. The aim is to examine the gas in lower-dimensional space and create traps with tailorable and dynamically tunable geometries. The experimental setup consists of a vacuum system with several components, as depicted in Figure 2.2. A high-temperature oven is used to reach the melting point of dysprosium atoms at $T \approx 1300^\circ\text{C}$. The hot jet of atoms heads towards the vertical two-dimensional magneto-optical trap (2D-MOT) chamber, where the atoms are slowed down and trapped in two dimensions by four crossing 421 nm laser beams, and a magnetic field. This confinement allows the atoms to move only along one horizontal axis. The 2D-MOT design is further described in [27] and [32]. A push beam transfers the atoms through a differential pumping stage into the science chamber, also called the main chamber, in an ultra-high vacuum environment with pressure below 10^{-11} mbar. The atoms are captured in a 3D-MOT consisting of six crossing 626 nm laser beams and a set of four coil pairs. Details can be found in [33], [34], and [35]. The science chamber itself is octagonal shaped and is made of stainless steel. It contains eight CF40 flanges on the sides and two CF100 flanges on top and bottom to ensure optical access for the imaging system. Four of the 3D-MOT beams enter the chamber from the sides and two from the top and bottom. In the summer of 2023, we further improved the setup and realized a 3D-MOT with only five instead of six beams by removing the top beam. The downward restoring force is provided by gravity, while the power

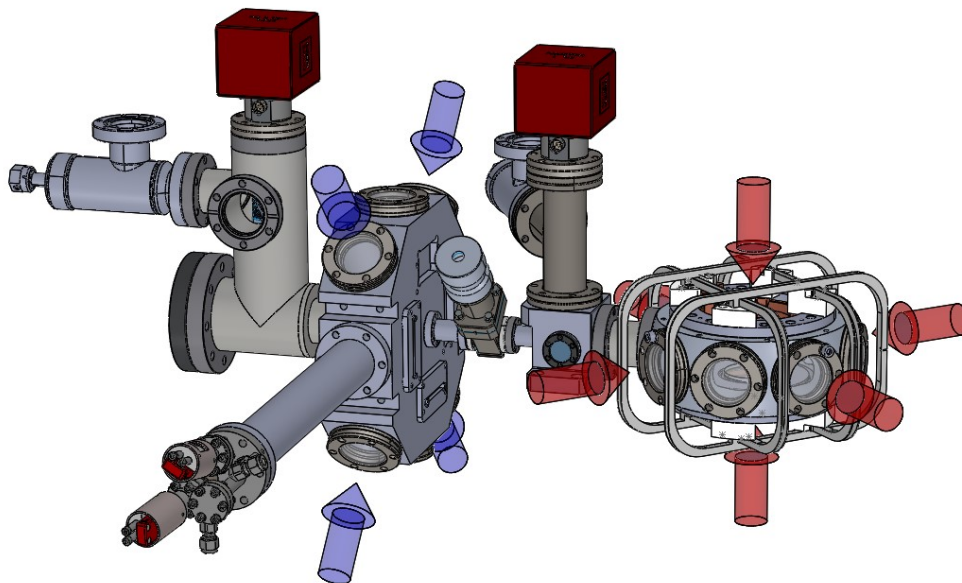


Figure 2.2: Experimental overview: The atoms from the hot jet produced in the high-temperature oven are captured in the 421 nm 2D-MOT (blue arrows), redirected to the main chamber and captured again in the 636 nm 3D-MOT (red arrows). From there, the atoms are loaded into an 1064 nm optical dipole trap and evaporative cooling is performed to reach the BEC regime.

and detuning of the vertical, upward propagating beam are adjusted in order to compensate for this effect. By decreasing the light detuning and intensity of the beams, the MOT is compressed. Afterward, the atoms are loaded into an optical dipole trap made of two crossing beams with a wavelength of 1064 nm [36]. Here, the evaporative cooling process is performed, where the depth of the trapping potential is reduced, which allows the most energetic atoms to escape from the trap. Due to interactions between the atoms, they thermalize and a new thermodynamical equilibrium emerges. The mean kinetic energy of the remaining particles is smaller, resulting in the reduction of the overall temperature of the system. Eventually, as the temperature drops low enough, a transition to Bose-Einstein condensation will occur. At this point, degeneration is achieved. The Bose-Einstein condensate is formed by a surfboard-shaped trap potential and can be further explored.

Four imaging setups along the horizontal axes are already included in the experiment

[37]. The main imaging system along the vertical axis that contains the microscope objective is currently in the building phase. It is mounted above the main chamber on an additional layer of breadboards. An imaging beam crosses the chamber and objective from below. This optical setup, as well as the absorption imaging technique and the implementation in the experiment, will be further explained in the course of this thesis.

The next steps to expand this setup in the near future are adding an accordion lattice to reduce the expansion of the atomic cloud to two dimensions, as well as adding a Digital Micromirror Device (DMD) for generating arbitrary trapping potentials. The accordion lattice setup will consist of two crossing 532 nm laser beams entering the main chamber from the side and creating sheets of light with variable spacing in the plane of the atoms. This is described in more detail in [38] and [39]. A DMD is an array of small mirrors that can be flipped individually to reflect light in or out of the optical path. Thereby, the intensity profile of a laser beam is modulated such that any potential can be projected onto the atoms. A more detailed description can be found in [40]. The DMD setup will be combined with the vertical imaging. Therefore, the coating of the microscope objective is chosen to be suitable for four different wavelengths in order to combine both optical systems.

2.4 Imaging Techniques

In cold atom experiments, the detection typically consists of imaging the gas density in two spatial directions. To determine the density distribution, different optical imaging techniques can be used, e.g. fluorescence imaging, absorption imaging, and phase contrast imaging. For fluorescence and absorption imaging, resonant light that shines on the atomic cloud gets absorbed and scattered due to spontaneous emission. In fluorescence imaging, the scattered light is collected from the side, while in absorption imaging, the shadow of the cloud is observed as a reduction in light intensity on the image compared to the beam itself. Fluorescence imaging is often used for single-atom sensitivity in a lattice due to its higher signal-to-noise ratio. However, absorption imaging provides more information about the whole cloud. On the other hand, phase contrast imaging relies on the dispersive phase shift that off-resonant light exhibits. The same effect of the light is used for dipole trapping. In general, imaging can be carried out in situ or in time of flight, where the atoms are released from the trap and

expand in free space. The velocity of the atoms can be calculated by measuring the traveled distance at a certain time. Hence, by varying the time of flight, the initial momentum distribution and, from that, its temperature is determined. The in situ images have a high atomic density compared to the time of flight method since the atomic cloud gets more dilute during the expansion.

Absorption imaging In the following, we will focus on absorption imaging. This method allows to capture spatially dependent images of the atomic density distribution by using the absorptive behavior of atoms on resonant light. The following explanation is adapted from [41] and [42]. For dysprosium, a beam with a wavelength of 421 nm can be used to drive the strong $\Delta J = 1$ transition. After the MOT compression, the cloud is fully spin-polarized in the lowest Zeeman sublevel $m_J = -8$ of the electronic ground state in all the subsequent experimental steps. Therefore, σ^- polarized light excites the closed transition from $m_J = -8$ to $m_J = -9$, while σ^+ polarized light excites the transition to $m_J = -7$, and π polarized light the one to $m_J = -8$. This is plotted in Figure 2.3. The axis of quantization is fixed along the magnetic field so in the direction of light propagation. The probabilities of excitation are given by the squares of the corresponding Clebsch–Gordan coefficients. A closed optical transition is required for a quantitative imaging scheme to avoid losses into dark states that can not be addressed by the imaging light and to be able to know the scattering cross-section of the imaging [43]. For dysprosium, the σ^+ transition is suppressed by a factor of about 150 and the π polarized one by a factor of about 10 compared to the σ^- driven one. Therefore, we can use in the experiment linearly polarized light parallel to the B-field direction for the vertical imaging to drive the σ^- transition and to achieve an effectively closed transition, while neglecting the σ^+ part of the light.

Due to absorption of the incident light, a shadow of the cloud is created and imaged onto the camera. If the incoming intensity I_{in} is sufficiently below saturation, the absorption is described by the Beer-Lambert law

$$\frac{I_{out}}{I_{in}} = e^{-\tilde{n}(x,y)\sigma_0}, \quad (2.2)$$

with the resonant absorption cross-section $\sigma_0 = \frac{3\lambda^2}{2\pi}$, wavelength λ , and outgoing intensity I_{out} after absorption. The column density \tilde{n} is the particle density $n(x, y, z)$ integrated over the z-direction $\tilde{n}(x, y) = \int n(x, y, z) dz$. The optical density (OD) of

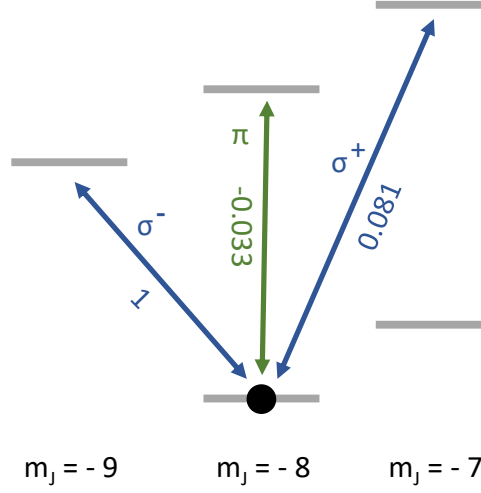


Figure 2.3: Simplified level scheme of the 421 nm transition in dysprosium. The $m_J = -8$ state represents the ground state, σ^- polarized light couples to the transition into the $m_J = -9$ state, σ^+ polarized light to the one into the $m_J = -7$ state, and π polarized light to the one into the $m_J = -8$ state. The Clebsch-Gordan coefficients are given for each transition.

the atomic cloud is defined as

$$OD = \tilde{n}(x, y)\sigma_0. \quad (2.3)$$

Saturation effects have to be taken into account for large intensities. They occur because a significant fraction of atoms becomes excited to higher energy states at high laser intensities. When a large fraction of the atomic population is already in an excited state, there are fewer ground-state atoms available to absorb additional photons. The absorption cross-section has to be replaced with a factor

$$\sigma_{sat} = \frac{\sigma_0}{1 + \frac{I_{in}}{I_{sat}}}. \quad (2.4)$$

The saturation intensity is then given by

$$I_{sat} = \frac{\pi}{3} \frac{hc\Gamma}{\lambda^3}, \quad (2.5)$$

with Planck constant h , speed of light c , and natural linewidth of the imaging transition

Γ. Including saturation effects, the Beer-Lambert law for absorption modifies to

$$\frac{dI(x, y, z)}{dz} = -n\sigma_{sat}I(x, y, z) = -n \frac{\sigma_0}{1 + \frac{I(x, y, z)}{I_{sat}}}, \quad (2.6)$$

where $I(x, y, z)$ is the intensity at position (x, y) of the imaging light propagating in z -direction [44]. Integrating Equation 2.6 along the beam direction yields the optical density

$$OD = -\ln \left(\frac{I_{in} - I_0}{I_{out} - I_0} \right) + \frac{I_{out} - I_{in}}{I_{sat}}, \quad (2.7)$$

where I_0 describes the constant background intensity on the camera. For intensities much smaller than the saturation intensity, the linear term can be neglected leading to the logarithmic Beer-Lambert law (2.2), which only depends on relative intensities[44, 45]. The second term dominates at high intensities when the transition is saturated. The intensities have to be known in units of the saturation intensity. From the optical density, also the column density of the atomic cloud can be determined with 2.3 by $\tilde{n}(x, y) = \frac{OD}{\sigma_{sat}}$.

In order to determine the optical density of the atomic cloud without introducing systematic errors due to the camera properties, a calibration process is carried out. It involves obtaining a set of three images that are used to establish a quantitative relationship between intensity profiles and OD. The first image is taken with atoms, measuring I_{out} . Two reference images are acquired, one without atoms, referring to $OD = 0$ and measuring I_{in} , and another one without the beam, referring to $I_{in} = 0$ with a constant background I_0 . With these three images and the saturation intensity, one can extract the optical density, which is independent on the camera characteristics. By subtracting the constant background I_0 , contributions from camera noise and residual background light are removed.

To be able to reconstruct the properties of the cloud from the images, the aim is to achieve an accurate determination of the local density. This is typically limited by the resolution of the imaging system, which will be introduced in 3.2. The imaging setup contains a microscope objective, lenses, and a camera to depict the atoms in the vertical direction. Since the atoms are located inside an ultrahigh vacuum system, one technical problems is the accessibility of the atoms. The components of the imaging system and its performance will be the topic of this thesis with a focus on the properties of the microscope objective that was custom designed to meet the requirements of the experiment.

3 Theory of Imaging and Simulation Principle

To understand the challenges, limitations, and potential of high-resolution imaging, it is important to first look at the physical principles of optics. This chapter will give a short introduction to the fundamental concepts, providing a basis for the subsequent discussion on the characterization of the microscope objective. Furthermore, the expected performance will be estimated by simulations based on those theoretical thoughts. The primary concepts of the theoretical background have been adapted from [46]. For the following considerations on very small objects with an extension close to the wavelength, geometric optics is not sufficient. In this regime, it is necessary to take the wave nature of light into account due to the diffraction limit. Understanding light as an electromagnetic wave with properties such as wavelength and frequency, described by the wave equation, are key principles. By taking into account diffraction and interference, the way light passes through materials or obstacles can be described. Since real optical systems come with additional imperfections, different types of aberrations will be introduced.

3.1 Fourier Optics

In Fourier optics, the propagation of light is described by Fourier analysis, considering the waveform as a superposition of harmonic wavefunctions. In the harmonic analysis, an arbitrary function $f(x)$ can be decomposed as an integral of harmonic functions of different frequencies and complex amplitudes:

$$f(x) = \int_{-\infty}^{+\infty} F(\nu) \exp(i2\pi\nu x) d\nu. \quad (3.1)$$

The component with frequency ν has the complex amplitude $F(\nu)$, which is the Fourier Transformation of $f(x)$, given by:

$$F(\nu) = \int_{-\infty}^{+\infty} f(x) \exp(-i2\pi\nu x) dx. \quad (3.2)$$

Equally, $f(x)$ is the inverse Fourier Transformation of $F(\nu)$. Therefore, if one of the functions is known, the other one can be calculated. A function $f(x, y)$ depending on the two spatial coordinates x and y can similarly be expanded as a superposition of harmonic functions of x and y . Here, $F(\nu_x, \nu_y)$ is the complex amplitude with the spatial frequencies ν_x and ν_y in the x- and y-direction, respectively. Two approximations for different regimes are often used in the analysis of diffraction patterns and wave propagation: The Fresnel approximation for near-field, and the Fraunhofer approximation for far-field diffraction. In the Fraunhofer regime, the incident light is effectively a plane wave with a constant phase and negligible curvature of the wavefront. This results in a simplification of the mathematical description when taking only linear terms into account. The diffraction pattern can be calculated as the Fourier Transform of the aperture function. For distances within a few wavelengths of the source, the Fresnel approximation is applied, where also second-order terms are considered. Both, the wavefront curvature and the propagation distance affect the phase of the wave and, in general, the integral can not be solved analytically. The near-field can be specified with the definition of the Fresnel Number

$$N_F = \frac{a^2}{\lambda d}, \quad (3.3)$$

with the distance d between the input and output plane, and the characteristic size a of the aperture. If the Fresnel number is small, $N_F \ll 1$, the Fraunhofer approximation is applicable. For values $N_F \approx 1$, the Fresnel approximation hold. For the regime of $N_F \gg 1$, the Fresnel diffraction pattern appears to be a shadow of the aperture, as it is expected in ray optics.

The spatial Fourier transform reveals the far-field distribution in the Fraunhofer approximation. By using a lens, this pattern can be revealed without a large propagation distance. Incoming parallel rays will be focused behind the lens to an imaging plane at a fixed distance f , the so-called focal plane. Therefore the diffraction pattern is brought from an infinitely large distance to the focal plane of the lens, which is then the Fourier plane of the incoming distribution. Each position in this plane corresponds to a certain spatial frequency of the input field before the lens. With a second lens, one can transform back into real space. The distance between the two lenses corresponds to the sum of their focal lengths f_1 and f_2 in order to form a sharp image. This two-lens imaging system is called a 4-f system, depicted in Figure 3.1. It can be understood as a cascade of two Fourier-transforming subsystems. The first lens transfers the input $f(x, y)$ from the object plane to its Fourier transform $F(\nu_x, \nu_y)$ in the focal plane at a

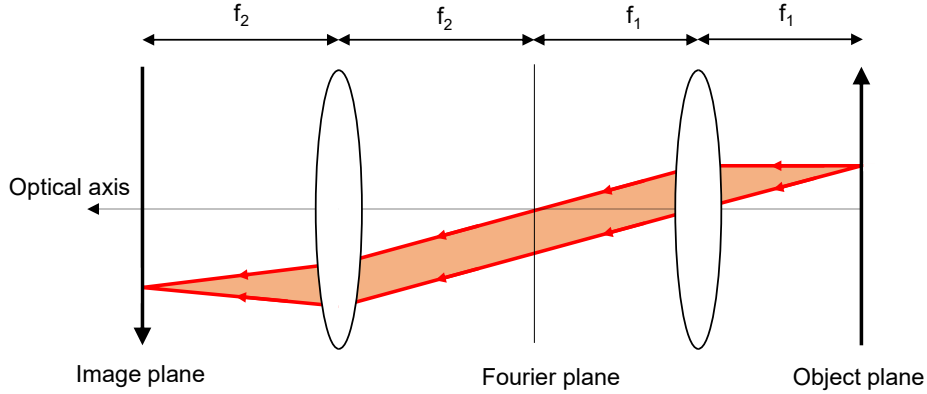


Figure 3.1: The 4f-system. Scheme of the two lenses placed with a distance of the sum of their focal lengths. The first lens performs a Fourier transform and the second lens performs an inverse Fourier transform. As a result, in the absence of an aperture, the image is a perfect replica of the object with a magnification factor of f_2/f_1 .

distance f_1 and separates its component in a way that every point in the Fourier plane corresponds to a single frequency:

$$x = \lambda f_1 \nu_x, \quad y = \lambda f_1 \nu_y. \quad (3.4)$$

The second lens represents the inverse Fourier transformation of $F(\nu_x, \nu_y)$ and produces the reconstruction $g(x, y)$ of the input at the imaging plane in distance f_2 by recombining the components. In an ideal system, this output $g(x, y)$ would be a replication of $f(x, y)$. It can be enlarged or reduced depending on the ratio of the characteristic lengths f_2/f_1 of the two lenses.

By placing an optical aperture in the Fourier plane, one can effectively modulate the spatial frequency spectrum. With a circular aperture centered on the optical axis, one can implement a low-pass filter, transmitting only components with sufficiently low spatial frequencies. Additionally, the finite size of a lens acts as an aperture and a low-pass filter as well. Thereby, the image $g(x, y)$ is only a filtered version of the object $f(x, y)$. To calculate the filtered Fourier transform $G(\nu_x, \nu_y)$ of $g(x, y)$ out of the original the Fourier transform $F(\nu_x, \nu_y)$ of $f(x, y)$, the transfer function $H(\nu_x, \nu_y)$ represents the mask in the Fourier plane:

$$G(\nu_x, \nu_y) = H(\nu_x, \nu_y) \times F(\nu_x, \nu_y). \quad (3.5)$$

The transfer function has the same shape as the aperture. Therefore, for a symmetric

circularly shaped mask, the transfer function for the effective low-pass filter reads as

$$H(\nu_x, \nu_y) = \begin{cases} 1 & \text{for } \nu_x^2 + \nu_y^2 < \nu_{cut}^2 \\ 0 & \text{else} \end{cases} \quad (3.6)$$

In this case, spatial frequencies up to the cut-off frequency ν_{cut} can pass, and higher frequencies are blocked. In the optical setup, this aperture has a diameter D defined by $D/2 = \nu_{cut}\lambda f$, where λ is the wavelength of the passing light.

3.2 Diffraction Limit

Any optical system has a theoretical limit for its resolution based on the principle of diffraction. It describes the bending of light waves when passing around an obstacle or through an aperture. Due to the wave nature of light, the diffraction pattern deviates from the geometrical shadow of the aperture, depending on the distance between the aperture and observation plane, the wavelength, and the dimensions of the aperture. The consequences of this behavior are an imperfect focus point and the formation of an interference pattern. In classical physics, this is described by the Huygens-Fresnel principle, which treats every point on a wavefront as a source of secondary spherical waves. In Fourier space, spatial frequencies can be blocked by apertures, as described before. This means only a part of the full feature of the pattern can be imaged. The diffraction phenomenon has significant consequences for the design and performance of optical systems.

The point spread function (PSF) describes how light from a point source forms an image after passing an optical system and is the inverse Fourier transform of the transfer function $H(\nu_x, \nu_y)$ of an imaging system. It characterizes the response of the system, and describes how the light is distributed in the image space. Due to diffraction, a point source of light cannot be perfectly focused onto a single point in the image. Instead, the light forms a characteristic pattern around the ideal point. This phenomenon directly impacts the system's ability to resolve fine details and produce sharp images. Furthermore, errors like lens imperfections and aberrations introduce more deviations. The point spread function serves as a valuable tool to characterize these effects and to understand their impact on the final image.

The smallest resolvable details, determined by the diffraction of light, are specifically

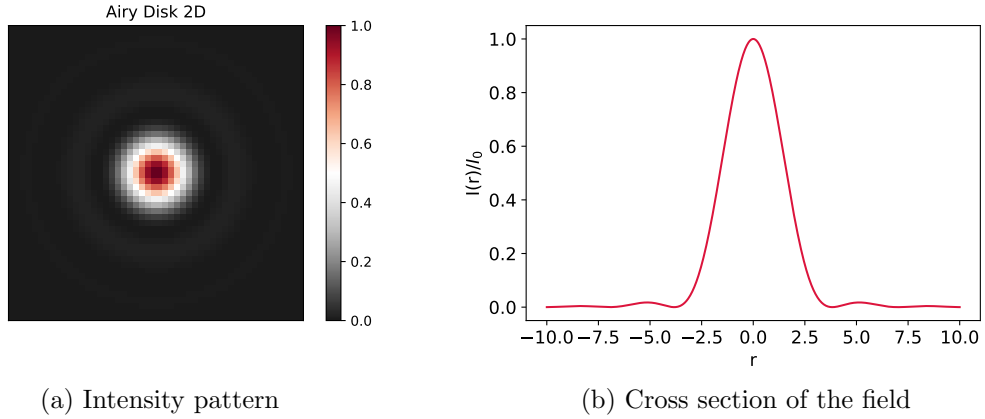


Figure 3.2: The Airy Disk pattern representing the Point Spread Function for circular apertures.

characterized by the Airy disk. It is a central bright spot surrounded by concentric rings of diminishing intensity that is observed when light is diffracted by a circular aperture, as shown in Figure 3.2. The intensity distribution depends on the distance R to the center of the aperture and is described by:

$$I(r) = I_0 \times \left(\frac{2J_1(\pi r)}{\pi r} \right)^2, \quad r = \frac{k a q}{\pi R}, \quad (3.7)$$

with the first order Bessel function J_1 , the circular wave number $k = \frac{2\pi}{\lambda}$, the wavelength λ , the radius a of the aperture, and the distance q between object and image plane. The size of the Airy disk is proportional to the wavelength of the light and inversely proportional to the diameter of the aperture. The angle θ , at which the first minimum of the Airy Disk is located, is given by the Rayleigh criterion

$$\theta \approx \arcsin \left(1.22 \frac{\lambda}{D} \right) \approx 1.22 \frac{\lambda}{D}, \quad (3.8)$$

with the diameter D of the aperture. The factor of 1.22 is often approximated as the first zero crossing point of the Bessel function J_1 . The angle θ defines the smallest angular separation between two point sources of light that can be resolved separately by the optical system. At this distance, the maximum of one Airy Disk is then located at the first minimum of the second. For a given aperture size, smaller wavelengths of light allow to resolve finer details, while larger wavelengths limit the achievable resolution. If two point sources are located closer than the diffraction limit, they will appear as a single blurred spot in the image. Therefore, the Rayleigh criterion defines

the theoretical limit of resolution for an optical system. This limit applies to all optical systems using light to form images. It provides a guideline for the smallest resolvable details that can be distinguished when imaging objects.

3.3 Aberrations

Every real optical system differs in some way from the theoretical ideal specifications. Accordingly, the produced image will deviate from the perfect performance. Such deviations are called aberrations. Several kinds of errors can occur, including blurring or deformation of the image. This is more precisely explained in [47], on which the following is based. Aberrations are caused by the lenses themselves or by misalignment of the system. By choosing optical parameters like refractive index, thickness, material, and distance of the lenses carefully, the aberrations can be minimized. They can also be corrected by placing apertures at certain positions in the optical path or by adjusting the optical path.

Spherical Aberrations For describing the trace of light through a lens or an optical system, the paraxial approximation is used. It assumes that the angle α between the light rays and the optical axis is small enough to justify a small-angle approximation $\sin(\alpha) \approx \alpha$. The rays that exhibit such a small angle are called paraxial rays. If this assumption is not fulfilled, non-paraxial rays influence the ability of the system to focus the light. Incoming light with a larger distance to the optical axis experiences stronger refraction towards the focal point. This phenomenon is called spherical aberration. This aberration is caused by the spherical shape of lens surfaces and is particularly problematic for lenses with a large aperture or wide field of view. It can be reduced by placing an aperture in front of the lens and thereby blocking the outer rays. However, this reduces at the same time the light intensity that passes through the system. Another option is the use of aspherical lenses, which are carefully shaped to eliminate or significantly reduce spherical aberration.

Coma For objects that are not located on the optical axis, a coma can appear. In this case, the incoming rays striking the lens under different angles are focused on different points along the optical axis. Coma aberration is particularly prominent when light rays pass through the edge of a lens, where the angle of incidence is higher, resulting in

different focal points for rays of varying angles. Objects appear distorted and show a characteristic tail that extends radially outwards from the central point source, similar to a comet. This aberration can be reduced by choosing the lens shape carefully and placing an aperture in the system, as well.

Astigmatism An aberration that causes distorted and stretched images is astigmatism. It occurs due to a difference in focal length along two orthogonal axes within the optical system. Light rays are not focused evenly in both the horizontal and vertical directions. This happens because the curvature or refractive power of the optical elements varies along different axes. The primary causes of astigmatism include irregularities in the shape of lens or mirror surfaces and asymmetry in the optical system. Point sources of light and objects with fine details appear stretched or distorted along certain directions. These distortions are more prominent in regions of the image far from the optical axis. It can be corrected in optical systems by using specialized optical elements, such as cylindrical lenses. Careful alignment and adjustment of optical components in the system can help minimize astigmatism.

Chromatic aberrations When using several wavelengths in one optical system, chromatic aberrations occur. Due to the dispersion of light, the diffraction is wavelength-dependent. Therefore, an optical system exhibits different focal points along the optical axis for different wavelengths. This results in the separation of focal points. Usually, shorter wavelengths are refracted stronger than longer wavelengths, leading to a closer focus for blue light than for red light. To address chromatic aberrations, achromatic lenses are designed by combining multiple lens elements made from different types of glass to bring different colors to a common focus.

Strehl ratio A parameter to describe the quality of an optical system's performance is the Strehl ratio. The Strehl ratio is a dimensionless number that ranges from 0 to 1, with 1 indicating perfect imaging. It is determined by comparing the actual performance of an optical system to an ideal diffraction-limited system. Mathematically, the Strehl ratio S is defined as the ratio of the peak intensity I_{actual} of the actual system to the peak intensity I_{ideal} of the idealized system:

$$S = \frac{I_{actual}}{I_{ideal}} . \quad (3.9)$$

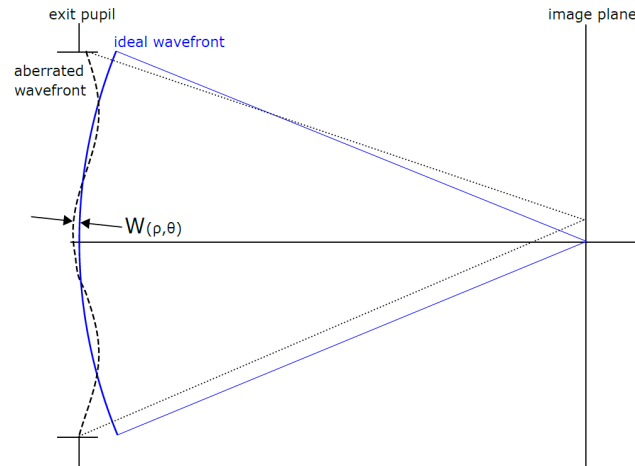


Figure 3.3: Comparison of an aberrated wavefront (dashed lines) to the ideal reference (blue). The optical path difference W is marked as path difference between the ideal and aberrated wavefront. The focus point on the image plane changes depending on the error sources. Figure taken from [48].

Following the Maréchal criterion, an image is practically indistinguishable from the aberration-free ideal when the Strehl ratio is larger than 0.82. This is a way to set a minimum acceptable level of image quality for an optical system and ensures that the optical system's performance aligns with the specific requirements of the application.

Wavefront aberrations The wavefront of a time-varying wave field is the surface of all rays having the same phase. For an ideal system, the wavefront of a point source of light is a perfect sphere, but it may have a distorted or irregular pattern for a real optical system [49]. This is depicted in Figure 3.3, where $W(\rho, \theta)$ indicates the optical path difference between a point on the ideal wavefront and the same point on the real, aberrated wavefront. To describe $W(\rho, \theta)$ of imaging elements with circular pupils, Zernike polynomials can be used. They are a sequence of polynomials with two variables that are continuous and orthogonal over a unit circle, first employed by Frits Zernike [50]. They are often expressed in polar coordinates (ρ, θ) , where ρ is the normalized radial coordinate ($0 \leq \rho \leq 1$) and θ is the polar angle ($0 \leq \theta < 2\pi$). This mathematical description is useful to describe the differences between the image formed by an optical system and the original object. These differences are caused by optical imperfections in the individual elements or the system as a whole.

The normalized Zernike circle polynomials $Z_n^m(\rho, \theta)$ are defined as the products of

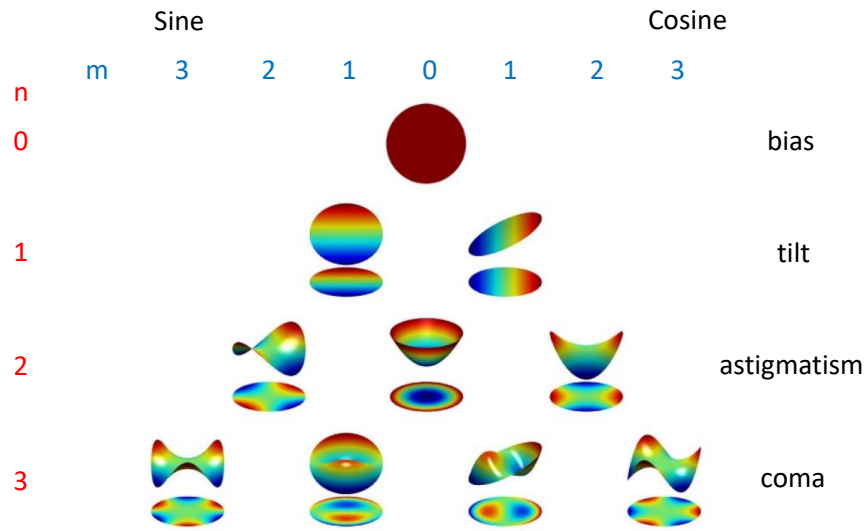


Figure 3.4: Pyramid of the Zernike circle polynomials. The indices n and m correspond to radial degree and azimuthal frequency. The aberrations associated with the polynomials are given. Figure adapted from [51].

normalization factors, radial polynomials, and azimuthal functions. The indices n and m correspond to radial degree and azimuthal frequency. They can be expressed in terms of the polynomial number j as $Z_j(\rho, \theta)$ corresponding to a combination of n and m to obtain a single index. For an even j , the corresponding polynomial is symmetric and for an odd j , the polynomial is anti-symmetric. In general, polynomials independent of θ describe spherical aberration, where $\cos \theta$ terms correspond to coma and $\cos 2\theta$ terms to astigmatism. Figure 3.4 shows the visualization of the Zernike circle polynomials up to the third degree, together with the classical aberrations that are associated with them.

3.4 Principle of the Simulations of our Imaging Setup

Based on the explained principles of Fourier optics, the test setup for the characterization of the microscope objective can be simulated by a 4-f system using Python. The structure of this is taken from [52]. The objective can be seen as a single lens with its focal length f_1 and aperture D as fixed properties. A second lens with focal length f_2 focuses the light rays into the image plane where a camera is positioned. The output

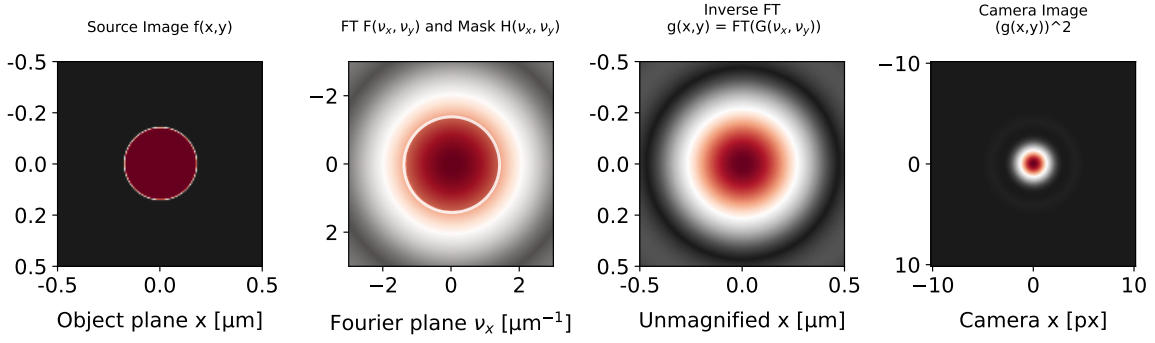


Figure 3.5: Structure of the Fourier Simulations. The left image shows the object plane with the 2D input function $f(x, y)$, followed by the Fourier plane with the Airy Disk distribution and the mask function $H(\nu_x, \nu_y)$ as white ring. The inverse Fourier transform of $G = H \times F$ results in the image in real space. The final output is determined by the magnification factor and the pixel size. The right picture shows the camera image $|g(x, y)|^2$.

function is magnified by a factor $M = f_2/f_1$, depending on the focal lengths of the two lenses. We chose $f_2 > f_1$ to achieve a magnification $M > 1$. A mask is applied in the Fourier plane by the limited aperture of the objective, which is described by a circle with fixed radius D . The cut-off frequency calculates to $\nu_{cut} = D/2\lambda f$ depending on the wavelength λ passing the system.

As input $f(x, y)$ of the 4f-system, a 2D array of pixels is generated in the shape of a top-hat function. It represents a uniform illuminated circular aperture as used in the experimental setup. This source image $f(x, y)$ is Fourier transformed to obtain the location of the components in the Fourier plane with using $F(\nu_x, \nu_y) = \int \int_{-\infty}^{\infty} f(x, y) \exp [i2\pi(\nu_x x + \nu_y y)] dx dy$. The first lens in the setup, which is the objective lens in our case, corresponds to this step. To achieve the intensity distribution of the illuminating light in the Fourier plane, the square $(F(\nu_x, \nu_y))^2$ of the Fourier Transform needs to be computed to obtain the diffraction pattern of the aperture. To take the limited size of the objective housing into account, the mask function $H(\nu_x, \nu_y) = 1$ for $\nu_x^2 + \nu_y^2 < \nu_{cut}^2$ and $H(\nu_x, \nu_y) = 0$ otherwise, describes a circle with radius $\nu_{cut} = \frac{D}{2\lambda f}$. By multiplying this with the Fourier transform of the input function, the low-pass filtered Fourier image $G(\nu_x, \nu_y) = H(\nu_x, \nu_y) \times F(\nu_x, \nu_y)$ is determined. The second lens performs an inverse Fourier transformation of $G(\nu_x, \nu_y)$, which leads to the calculation of the output $g(x, y) = \int \int_{-\infty}^{\infty} G(\nu_x, \nu_y) \exp [-i2\pi(\nu_x x + \nu_y y)] d\nu_x d\nu_y$ at the image plane. The intensity of the light that hits the camera is described by the square $|g(x, y)|^2$, eliminating the negative values. This represents the actual light intensity

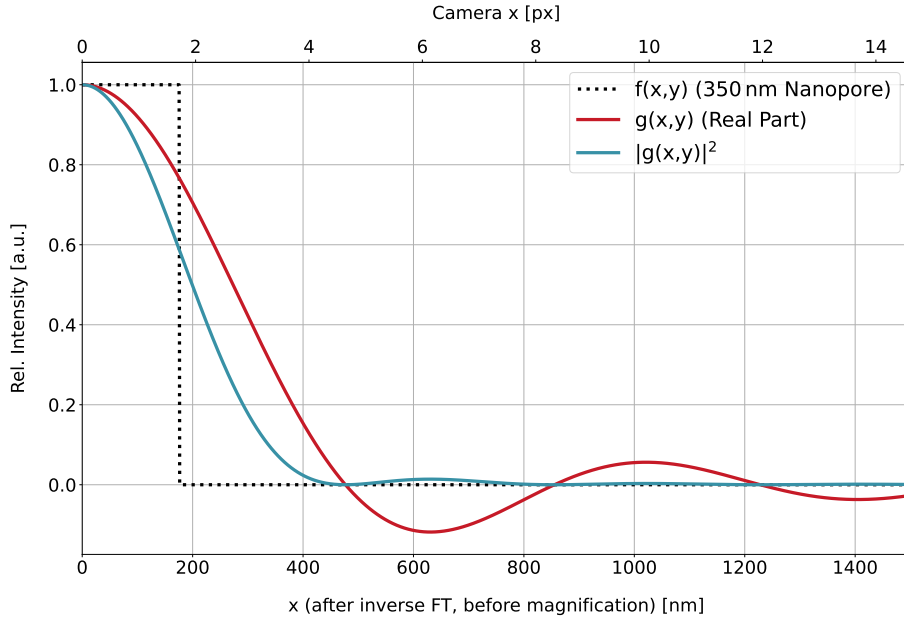


Figure 3.6: Cross section of the 2D simulation with 421 nm. The dashed line indicates the top-hat function that is used as input for the simulations. The red curve shows the light field after the second Fourier transformation and the blue curve is the squared amplitude representing the camera image. The lower x-axis does not include the magnification of the 4f setup yet and has units of micrometer, while the top axis labels are in units of camera pixel, including the magnification.

distribution on the camera sensor. The size of this camera image will be scaled by the magnification M of the system and the pixel size d_{pixel} of the camera.

The output of the simulations is the 2D intensity distribution, which will be visible on the camera, as shown in Figure 3.5. The 1D cross-section is depicted in Figure 3.6, corresponding to the intensity after the 4f setup. The first zero of the output function determines the resolution of the setup. It is larger than the radius of the input function and depends on the wavelength of the laser beam. The given size of the input meets the dimensions that will be used in the experimental setup. The intensity is normalized to its maximum since the radius is independent of the amplitude of the peak. The size of the radius on the camera depends on pixel size and magnification. The 2D pixel plot and 1D cross-section provide an expectation for the test measurements that can be adjusted for the different wavelengths of interest.

Defocus calculations Up to now, the simulation cannot describe the defocus behavior. This means that the distance between the object plane and the first lens does

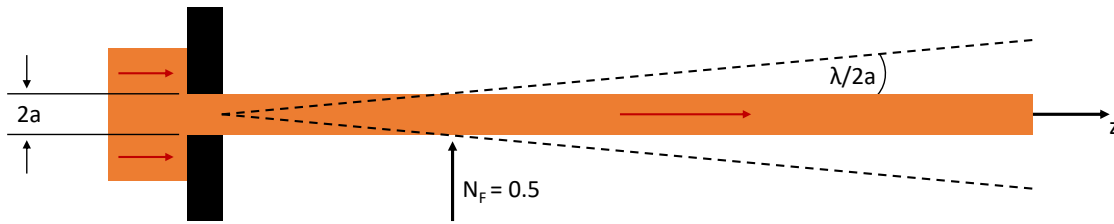


Figure 3.7: Diffraction from a slit of width $D = 2a$ with light propagating in z -direction. The shaded area represents the geometrical shadow of the aperture. The dashed line is the width of the Fraunhofer diffracted beam in the far field. Where the dashed lines coincide with the edges of the geometrical shadow, the Fresnel number $N_F = \frac{a^2}{\lambda d} = 0.5$ with distance d between input and output plane. Larger distances corresponds to smaller Fresnel numbers.

not match the theoretical value but is shifted along the beam propagation axis. An approach to include this in the simulations is to use an altered input function for the algorithm. Therefore, the light propagation from the original object plane to the shifted one has to be calculated. It takes a spatial path with the length of the translation that can be set individually. The function that describes the light after propagating to the new object plane is taken as a new input function for the Fourier transform series. Different approaches are possible to calculate the light propagation depending on the distance to the origin. The Fresnel number gives information about the approximation that can be used in the specific regime. At very small distances, which means large N_F , the diffraction pattern is a perfect shadow of the slit. When the distance increases, N_F decreases, and the wave nature of light leads to oscillations around the edges of the aperture. For a Fresnel number smaller than 0.5, the width of the Fraunhofer diffraction is larger than the geometrical shadow of the aperture, as can be seen in Figure 3.7. For the given conditions in the region of interest, the Fresnel number ranges around $N_F = 0.1$ leading to the far-field regime, where the Fraunhofer pattern is obtained. The pattern can be calculated for certain distances and taken as new input for the 4f-system simulations. This describes the translation of the object along the optical axis in the range of micrometers. From calculating the radius of the output function for different distances to the object plane, the defocus behavior of the system is predicted to be linear. This means the PSF radius increases linearly when shifting the objective out of the focus plane. The slope of this depends on the wavelength and aperture size. This will be further discussed in Section 5.4.4 with the defocus measurements.

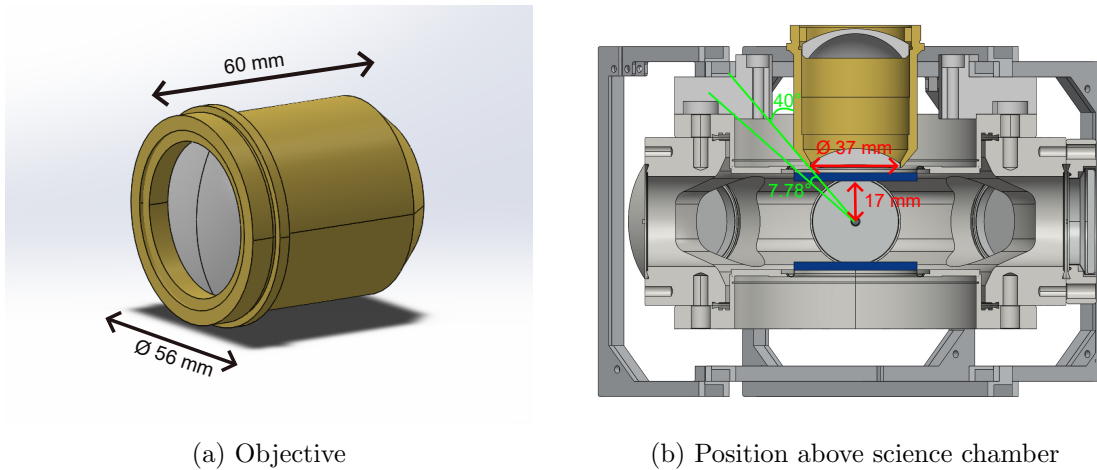
4 Design of the Objective

The heart of the high-resolution imaging setup is the microscope objective. It is custom-designed by the company Special Optics. The optical design of the objective incorporates advanced lens elements and coatings that minimize aberrations and allow for capturing small details while maintaining minimal distortion across the image. These are considerations to achieve exceptional resolution and define, to some extent, a lower boundary for the diameter of the lenses and the physical extent of the housing. Additionally, the mechanical constraints of the setup must be adhered to in order to ensure the objective can be integrated into the experiment. This means that an upper limit to the overall size of the objective, as well as other length scales, are fixed and have to be kept in order to ensure proper integration into the experimental setup. These two contrasting requirements have to be balanced in a way that the minimum necessary but maximal possible size of the objective is chosen. In the following section, the specific properties of the microscope objective will be discussed. Explanations of general properties are based on [53], which gives an introduction to optical microscopy.

4.1 Mechanical Design

The objective will be placed above the science chamber and has to fit between the coil holder, which limits the size of the housing. Furthermore, this requires a fully non-magnetic and non-conductive material for the housing. It is manufactured of Ultem¹ with an outer diameter of 52 mm and an overall length of 60 mm. The mounting thread on the back is 7.5 mm long with a diameter of 55 mm. In the front, there is a diagonal cut-off at an angle of 40° to ensure an unobstructed view of the main chamber. This is depicted in Figure 4.1. More details on the mechanical design can be found in the Appendix A.1. The 52 mm outer diameter strikes a balance between maximizing the aperture for light collection and fitting within the available space to accommodate the constraints of the surrounding, while maintaining optimal performance. The mounting

¹Ultem® 2300 PEI-30



(a) Objective

(b) Position above science chamber

Figure 4.1: The microscope objective housing is shown as a 3D simulation with its total length of 60 mm and diameter of 56 mm. On the right, the position above the science chamber is illustrated. The atoms are positioned in the middle of the chamber with a distance of 17 mm to the viewport that has a thickness of 3.505 mm. Due to the 40° cut-off angle at the objective, a view of the main chamber with an angular size of 7.78° remains unobstructed.

thread allows secure attachment, which is particularly important since the objective lens will be installed from the upper breadboard. Therefore, mechanical stability has to be ensured through the design.

4.2 Working Distance

The working distance (WD) of an objective refers to the distance between the first lens of the objective and the focal plane. While the focal length is an intrinsic property of a lens related to its optical behavior, the working distance is an extrinsic parameter. It is affected by the arrangement of lenses inside the objective housing and has to match the space, which is available in the experiment. A microscope objective for high-resolution imaging would usually have a rather small working distance to be able to collect light from large angles while having a limited aperture diameter. In the setup is the minimal distance to the focal plane already fixed by construction with a distance of 17 mm from the middle of the chamber to the viewport in vacuum and a thickness of the viewport of 3.505 mm. To have a tolerance for mounting and adjusting, another 2 mm in the air are added, resulting in a working distance of $WD = 17 \text{ mm} + 3.505 \text{ mm} + 2 \text{ mm} = 22.505 \text{ mm}$. This value was set by the mechanical conditions and sets the first constrain.

4.3 Numerical aperture

The numerical aperture (NA) is a dimensionless number that describes the range of angles where light can be gathered by the system based on geometric considerations. It is calculated by the formula

$$\text{NA} = n \times \sin \theta, \quad (4.1)$$

where n is the refractive index of the medium in which the lens operates and θ is the half-angle of the maximum cone of light that can enter the objective. It is schematically depicted in Figure 4.2. A higher numerical aperture corresponds to a larger cone of light entering the objective. This means that the objective can capture more light, resulting in a brighter and more detailed image. It determines other parameters like resolution, depth of field, and image brightness and is crucial for the performance of the whole system. The numerical aperture of the Special Optics objective is set to be $\text{NA} = 0.6$, which corresponds to an angle of $\theta = 36.8^\circ$. This property was the key requirement for the whole system, to ensure high resolution for the imaging. All other characteristics were secondary and had to be adjusted to achieve the best possible performance.

4.4 Focal Length

The focal length is a fundamental optical property that describes the ability of a lens to converge or diverge passing light rays. For positive values, the light converges and the focal length indicates the distance it takes to focus initially parallel light rays. On the other hand, for negative values, the light diverges. A negative focal length is the distance in front of the lens at which a point source subsequently forms a collimated beam. When choosing the focal length, a balance must be found between magnification, field of view, and optical performance. The focal length of the microscope objective determines the magnification of the imaging setup, as further explained in Section 4.5. Shorter focal lengths correspond to higher magnifications, while longer focal lengths correspond to lower magnifications. For a system with several lenses acting together, one effective focal length describes the entire system. The effective focal length of the custom-designed microscope objective is $f_{\text{objective}} = 32.2 \text{ mm}$.

4.5 Magnification

High-resolution microscope objectives are often infinity corrected, which means they use parallel light beams instead of focusing the intermediate image to simplify the optical design, enhance image quality, and provide more flexibility. This simplifies the mechanical design because any optical element placed after the objective can manipulate the parallel light without inducing significant focus shifts. Infinity correction provides the flexibility to introduce components between the objective and camera, such as filters, beam splitters, and other accessories, with minimal impact on the image quality. Additionally, it reduces optical aberrations introduced by other components. The design is well-suited for coupling microscopes with imaging devices like cameras or digital sensors. Parallel light beams are directed onto these devices through an additional lens, which focuses the collimated beam onto the image plane without significant loss of image quality. The overall magnification M of the optical system is determined by the focal length f_{lens} of this additional lens placed behind the microscope objective and can be calculated by

$$M = \frac{f_{lens}}{f_{objective}}. \quad (4.2)$$

Since the focal length of the objective is fixed, only the focal length of the lens can be varied to reach a suitable ratio. This has to be chosen in a way that the aimed area can be depicted with sufficient precision. For a larger magnification, a sufficient number of photons per pixel has to be detected on the camera to ensure an atom signal higher than the camera noise. In the experiment, we aim for a value of approximately $M = 20$ to meet those requirements. With a pixel size of $4.6 \mu\text{m}$ of the camera used in the experiment, the effective area of one pixel is $0.23 \mu\text{m} \times 0.23 \mu\text{m}$. The overall area that can be depicted will be about $942 \mu\text{m} \times 392 \mu\text{m}$.

4.6 Back Focal Plane

At the back focal plane, incoming parallel light rays converge after passing through the objective. Behind this plane, the beams are highly diverging. For a defocusing system, the back focal point can be a virtual point located on the front side. Some interesting features like the Fraunhofer diffraction and the Fourier transform of the image are located there. It is situated on the back side the lens opposite to the focal plane and lies often inside of the lens system. However, for this objective, effort was

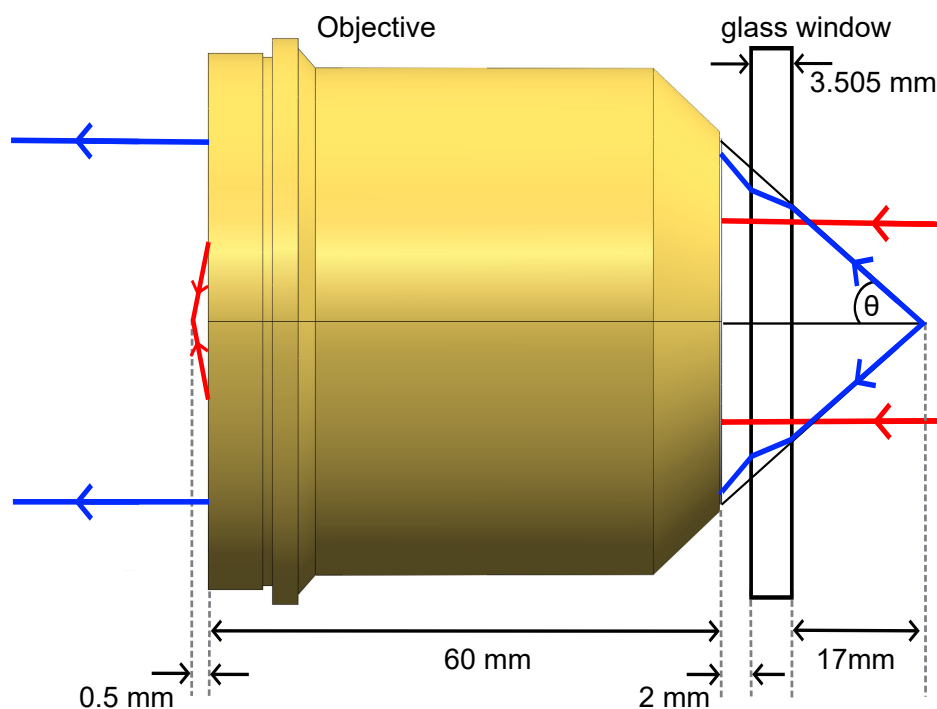


Figure 4.2: Focus and backfocus of the objective. Blue lines indicate light originated in the working distance that leaves the infinity corrected objective collimated. Red lines indicate parallel incoming rays, that are focused in the backfocal plane. The rectangular on the right represents the glass viewport of the science chamber. The angle θ is the maximum angle at which light can enter the objective determining the numerical aperture.

made to position it outside of the housing. It is located approximately 0.5 mm behind the last lens. Shifting the back focal plane to an external position allows to place other optical components, which leads to a more adjustable design. The position of the focus and backfocus plane is schematically depicted in Figure 4.2. The parallel incoming beams from the right are focused close to the surface of the objective housing on the left. The focus plane on the right is positioned at the working distance of 22.505 mm, as described in 4.2. This also includes the 3.505 mm thick glass window shown in Figure 4.2. Light beams that originate at the focus plane leave the infinity-corrected objective parallel on the left.

4.7 Resolution

The objective is diffraction-limited to the four wavelengths of 421nm, 532nm, 626nm, and 1064nm that are used in the experiment. Achieving diffraction-limited performance

Wavelength	PSF radius	depth of field
421 nm	428.01 nm	0.4667 μm
532 nm	540.87 nm	0.5906 μm
626 nm	636.43 nm	0.6950 μm
1064 nm	1081.73 nm	1.1812 μm

Table 4.1: Minimal PSF radius by Rayleigh criterion and depth of field calculated for the four wavelengths of interest, respectively.

means that the system reaches the theoretical limit of resolution, described in Section 3.2. Therefore, the details of the produced images are limited only by the diffraction of light itself and not by optical aberrations or other imperfections in the system.

For a microscope, the minimal PSF radius r_{theo} can be calculated from equation 3.8 with the definition of the numerical aperture NA in equation 4.1 as

$$r_{theo} = \frac{1.22}{2} \frac{\lambda}{\text{NA}} = 0.61 \frac{\lambda}{\text{NA}}. \quad (4.3)$$

If the separation between two objects is smaller than this limit, they will appear blurred and merged in the image. From equation 4.3, the theoretical value for the radius of the point spread function can be determined for the four wavelengths of interest, as depicted in Table 4.1. Overall, the image quality of the optical system is also influenced by other components of the microscope system, including the quality of the optics, illumination sources, and detectors.

4.8 Depth of Field

The depth of field is the distance in front of and behind the focused plane that can depict objects still in focus on the imaging sensor. Since it is measured parallel to the optical axis, another description is axial resolution. For microscopes, the depth of field is in the micrometer region. It is determined by the numerical apertures, while a higher value results in a shallower depth of field. Since higher NA objectives capture more light the effects of diffraction are increased and, thus, the depth of field is reduced. From the Rayleigh criterion (Eq. 4.3), the depth of field (DOF) is calculated in first-order approximation to

$$\text{DOF} = \frac{\lambda \sqrt{1 - \text{NA}^2}}{2 (\text{NA})^2}. \quad (4.4)$$

This means that up to this spatial distance orthogonal to the focal plane, the radius of the point spread function is still at the minimal theoretical value. The values for that can be found in Table 4.1. If an object or aperture is positioned at a larger distance than the focal plane, the light first spreads out from there to the focus plane. The light is imaged from there by the objective. The input is then bigger than originally and will be depicted on the image plane as an enlarged picture. As explained in 3.4, calculating this with the Fourier simulations of the setup leads to a linear growth of the point spread function radius. The slope of the curve depends on the wavelength and the size of the aperture. This is only valid in the Fraunhofer regime.

4.9 Field of View

The field of view (FOV) is the area in the focal plane, perpendicular to the optical axis, where the required parameters are fulfilled, which is understood as a Strehl ratio below 0.82 (see 3.3). It is circular shaped and has a diameter in the order of micrometers to millimeters. Objects positioned inside the field of view can be imaged without larger aberration effects, while light from outside will be distorted stronger. The size of the field of view is primarily determined by the optical design, magnification, and aperture of the objective. Typically, higher resolution objectives have smaller fields of view because they maximize the image quality in the central part of the object plane, while outer regions exhibit stronger optical aberrations. The Special Optics microscope objective has a field of view diameter of $200\ \mu\text{m}$ for all wavelengths of interest.

4.10 Chromatic focal shift

For high-resolution imaging, already small aberrations have an impact on the image quality. The chromatic focal shift is of particular interest for the setup. As described in 3.3, this is the optical phenomenon of different distances between the focal point and the objective along the optical axis for different wavelengths. This effect can be minimized or corrected using techniques such as achromatic lens designs and coatings, carried out by Special Optics without participation from our side. While these techniques reduce chromatic focal shift, complete elimination is not possible. Due to the dispersion of light, the refractive index of the lens elements varies with the wavelength of the light. Therefore, the design must strike a balance between achieving optimal color

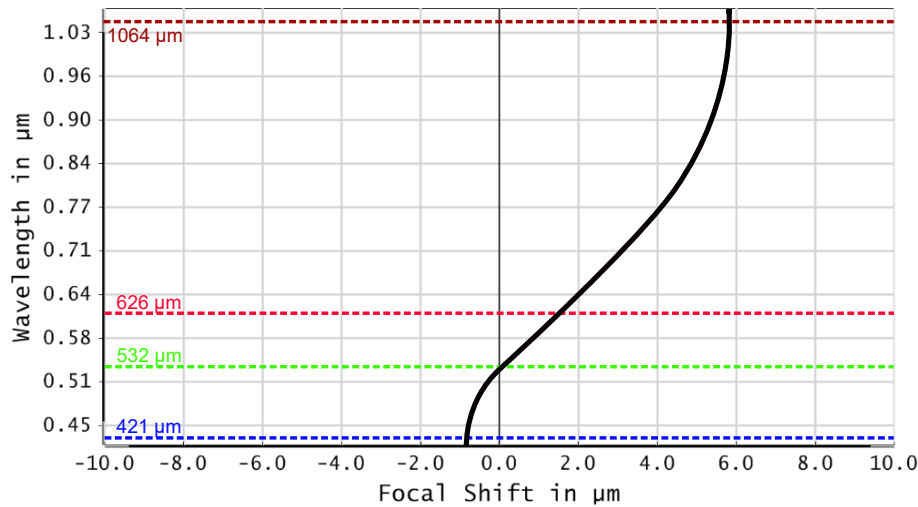


Figure 4.3: Chromatic focal shift of the microscope objective for the chosen wavelengths, calculated with Zemax. The dashed horizontal lines highlight the wavelengths of interest.

shift and addressing other optical considerations, such as resolution and field of view. The objective is designed to minimize chromatic aberration over the chosen range of wavelengths. For the chromatic focal shift, an upper limit of $10\ \mu\text{m}$ is set for this range. The exact behavior for the wavelength region of interest is depicted in Figure 4.3. With respect to $532\ \text{nm}$ as zero point, the largest deviation occurs at $1064\ \text{nm}$ with around $6\ \mu\text{m}$. The other two values, $421\ \text{nm}$ and $626\ \text{nm}$, lie within a $2\ \mu\text{m}$ interval, respectively.

4.11 Transmission

The transmission of a lens refers to the amount of light that passes through the objective and reaches the image plane. It quantifies the efficiency of transmitting light without absorption or scattering. This impacts the overall image brightness and contrast. It can be influenced by various factors, including lens coating quality (which can reduce reflections and increase transmission), the type of glass or materials used in the lens construction, the design of the lens elements, and the wavelength of the passing light. This lens processing is fully done by Special Optics. By calculating the ratio of outgoing to incoming intensity, the transmission coefficient of the objective lens can be calculated. The transmission coefficient is a dimensionless number between 0 and 1, indicating the fraction of incident light that successfully passes through the lens. For

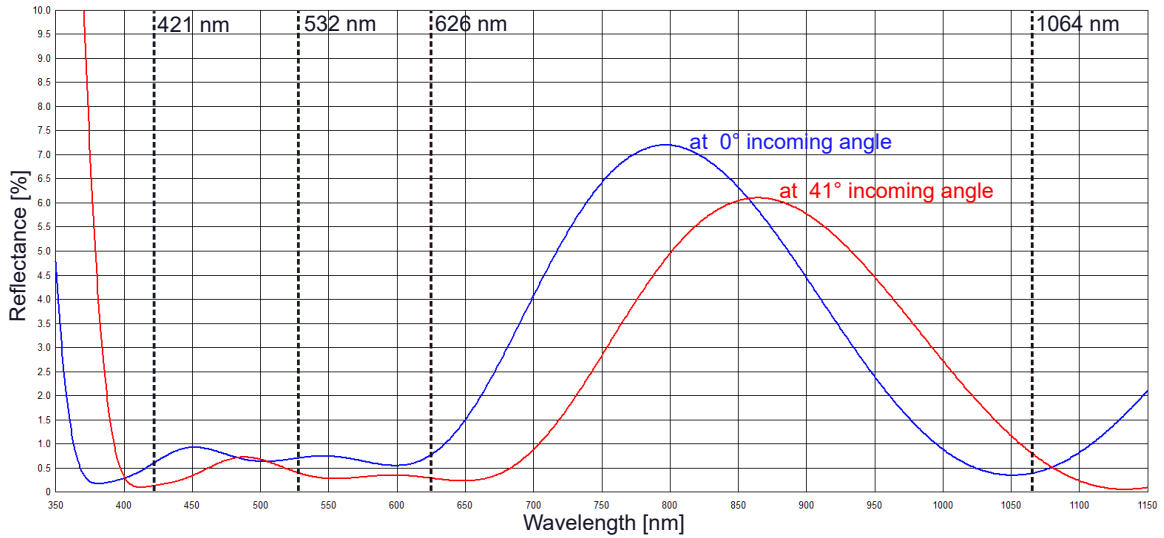


Figure 4.4: Coating curves of the microscope objective. The blue line indicates the reflectance at an incoming angle of 0° , the red curve of 41° . The wavelengths of interest are highlighted by the dashed lines. This plot was provided by Special Optics.

Wavelength	Transmission Coefficient
421 nm	> 0.78
532 nm	> 0.86
626 nm	> 0.86
1064 nm	> 0.86

Table 4.2: Expected transmission coefficients for the four wavelength, given by Special Optics.

a value of 1, all energy of an incoming wave passes through the material while for a value of 0, the light is entirely absorbed or reflected. The transmission coefficients for this microscope objective, given by Special Optics, are shown in Table 4.2.

Additionally, the light's angle of incidence on a lens is a crucial factor that affects the transmittance and reflectance of the lens. This phenomenon is described by the principles of electromagnetic optics. The angle at which light enters the lens relative to the normal perpendicular to the lens surface is called the angle of incidence. When light enters a lens at an angle, it may experience different levels of refraction depending on the angle and the refractive index of the material. Therefore, it is crucial to design lenses, which minimize the impact of aberrations caused by varying angles of incidence. A complex lens design with multiple lens elements can be used to correct for these effects. For the experiments, the angles of interest are between 0° and 41° , since this is

the cone in which light will hit the objective lens. In Figure 4.4, the reflectance of the objective is shown for an incoming angle of 0° and 41° as a function of the wavelength. For the wavelengths of interest, marked by dashed lines, the reflectance is chosen as low as possible with values below 1% for both angles. At 421 nm, the behavior is optimized with $<0.25\%$ reflectance for 0° incoming angle and $<0.75\%$ for 41° , respectively. This behavior is determined by the anti-reflection coating that was applied by Special Optics in order to achieve the best possible result for the given requirements of the experiment.

5 Experimental Realisation

So far, only theoretical predictions of the objective's performance have been presented. Next, this will be tested in reality by characterization measurements, which refer to the process of quantitatively assessing the properties of the objective. This involves collecting data and analyzing the results to gain insights into the different aspects that play a role in image formation. By conducting these comprehensive tests and evaluations, one can ensure that the microscope objective performs as expected and gain insights into its capabilities, limitations, and optimal usage. In order to characterize the objective and perform measurements on the specified properties, a separate test setup is useful. It should simulate the requirements in the experiment as close as possible. Therefore, length scales, distances, and available degrees of freedom were chosen accordingly. In this chapter, the test setup with the used components and their properties will be described as well as the results of the characterization. Important parameters are resolution, field of view, depth of field, and focal shift. In addition, the alignment procedure was tested and optimized.

All measurements were conducted with four wavelengths: 405 nm, 532 nm, 635 nm, and 1064 nm. They are close to the ones in the experiment, for which the microscope objective is optimized. Some parts could not be included in the test setup, for example, the custom-designed mount for the objective or the camera of the experiment. The direct transfer between characterization in the test setup and performance in the experiment is limited by these elements. After finishing the characterization and implementing the objective in the experiment, we found that some more measurements would have been good to include. The actual orientation of the microscope in the experiment is vertical, while it was placed horizontally in the test setup. The performance of the stages, when working in the direction of gravity, was not measured. This has an impact on the step size, which differs for moving upwards and downwards. The design of the actual mount was not finished when building the test setup. Therefore, a simpler version of it was used and the final one was not tested. Additionally, a more quantitative estimate of the tilt angles between objective and viewport would have been useful.

5.1 Test Setup Design

In the following description, the chosen coordinate system treats the optical axis as the z-axis, where the positive direction refers to the beam propagation. The definition of the reference can be found in Figure 5.1. For convenience of operation, the z-axis is horizontal in the test setup. This is contrary to the experimental implementation in Chapter 6, where the z-axis is vertical. The setup consists of a resolution target¹ to simulate the atomic cloud in the experiment. It consists of a quadratic 5 mm long silicon frame. Inside, a silicone nitride membrane with a size of 0.3 mm x 0.1 mm is fixed. It has a thickness of 50 nm and a coating with 5 nm chromium and 50 nm gold on both sides. In the middle, two nanopores are positioned. They have a pitch of $7\mu\text{m}$ and each has a diameter of 350 nm. The target is glued on the opening hole of a fiber adapter², which itself is screwed into a lens tube. An optical fiber is attached on the other side of the tube in a fiber adapter of the same kind. The tube itself is mounted on a three-axis translation stage³ that can be controlled remotely by a piezo motor. It moves in x-, y-, and z-direction with a step size of $1\mu\text{m}$ and a range of 20 mm. As light sources, four laser diodes⁴ with a power of 5 mW are used for the different wavelengths, coupled into the mentioned fiber. After a distance of 17 mm, a glass window with a thickness of 3.505 mm and a diameter of 48 mm is mounted to simulate the viewport. Therefore, the distance between target and glass window corresponds to the same distance of 17 mm between the atomic cloud and the viewport of the vacuum chamber in the main experiment.

The microscope objective is mounted on two stages to ensure all necessary degrees of freedom. The distance is chosen in accordance with the working distance of 22.505 mm. Between the objective and glass window are 2 mm of free space. The lower stage translates the objective in z-direction⁵ with a range of 25.4 mm. The piezo controller⁶ has a step size below 30 nm. On top, a four-axis stage⁷ is mounted via a self-designed adapter plate. It translates and tilts the objective in x- and y-direction with a travel range of 3 mm and an angle range of 8° , respectively.

To magnify and focus the image on the imaging plane, a plano-convex lens with a

¹Norcada Nanopore Products

²Thorlabs SM1FCA2 - FC/APC Fiber Adapter Plate

³Thorlabs ORIC® 20 mm Linear Translation Stage ORIC® 20 mm Linear Translation Stage

⁴Roithner Lasertechnik CW405-05, CW532-005, LDM635/LJM, and CW1064-05

⁵Newport 9063-X-P-M Motorized Gothic-Arch Bearing Stage with Picomotor™ actuators

⁶Newport 8742-4-KIT Picomotor Controller

⁷Newport 9071-M Four-Axis Tilt Alignment Stage

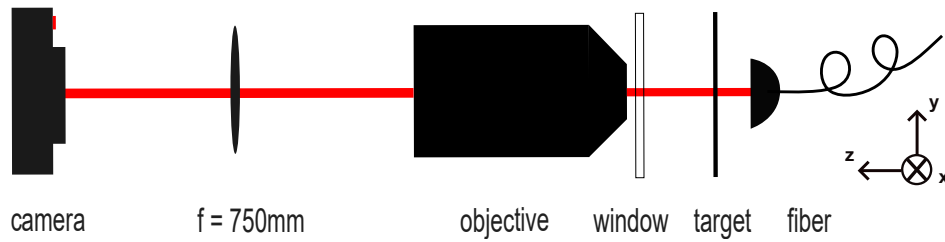


Figure 5.1: Scheme of the experimental test setup for the characterization.

focal length of 750 mm and a diameter of 50.8 mm is placed on a five-axis stage⁸. The 4f-system introduced in 3.1 follows. The stage translates in all three linear directions with a range of 3 mm and rotates around the x- and y-axis with a range of 8°.

At the focal point of the lens, a CMOS camera⁹ is placed. It has a sensor size of 1440 x 1080 pixels with a pixel size of 3.45 μm . For the measurements with 1064nm, the quantum efficiency is not sufficient. Therefore, a different camera has to be used. Here, a beam profiler¹⁰ with a wavelength range of up to 1150nm was used. The optical path of the setup is schematically depicted in Figure 5.1. A beam height of 100 mm above the optical table is suitable for the mounting of all optical elements within the setup.

For more stability of the objective and the resolution target on their stages as most sensitive parts, an additional plate was designed. This breadboard can be fixed on the optical table with M6 screws and provides a base plate for positioning the components. It contains inlets for the stages of the target and objective, as well as the glass window (see Fig. 5.2). The thickness of the board is 15 mm, so the beam height of the components on the breadboard is 85 mm. The one-axis linear translation stage is directly fixed in the inlet with four M6 screws, while an adaptor plate connects it with the four-axis stage mounted above. Another adaptor allows to screw the objective mount on the upper plate. The housing of the objective itself has a thread that ensures proper attachment. The glass window lies on a smooth recess and is fixed by a two-inch ring. This ring is screwed into a thread in the holder, which is fixed on the respective inlet in the plate. The three-axis stage is just fixed on a rectangular solid that itself is fixed on the breadboard in its own inlet. The tube with the resolution target is fixed on the vertical surface of the stage.

The stages used in this setup are open-loop. This means no feedback system is implemented, such that the step size depends on the workload and may differ in space and

⁸Newport 9081-M Five-Axis Tilt Alignment Stage

⁹Thorlabs CS165CU/M - Zelux® 1.6 MP Color CMOS Camera

¹⁰DataRay WinCamD-LCM – 1" CMOS Beam Profiler

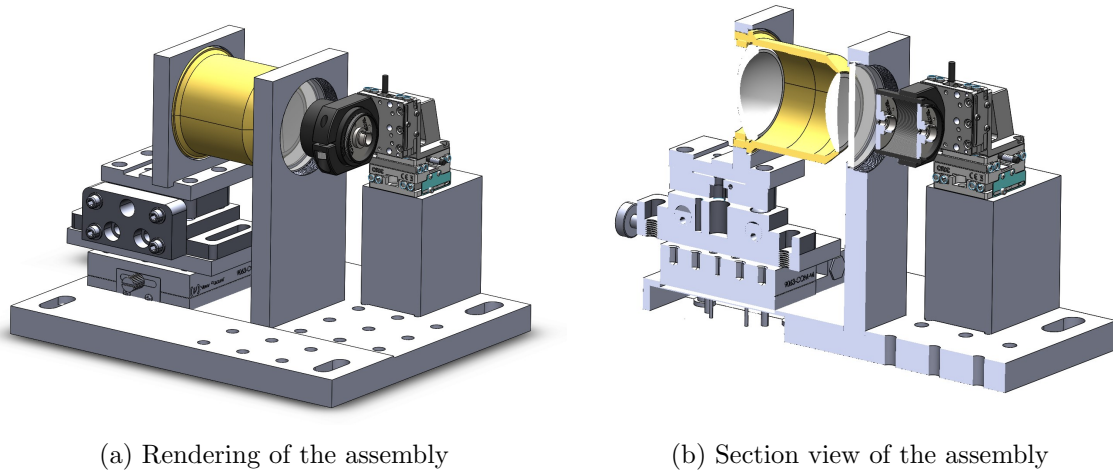


Figure 5.2: Breadboard of the test setup, including the stages and mounts, as well as objective, glass window, and resolution target. Technical Drawings can be found in Appendix A.1.

over time. In the setup, the weight on the stages was constant, but a deviation of the movement in different directions was observed, particularly for shifting the target in the y -direction. This had to be taken into account for the handling during the measurements. Therefore, the position of the target after moving the stage was checked on the camera. Using closed-loop stages instead could provide more stability and reduce uncertainty.

5.2 Alignment

Proper alignment of the objective is crucial for accurate imaging. Misalignment can cause aberrations, resulting in reduced resolution and the inability to distinguish fine details. Several steps were carried out to adjust the different components of the test setup step by step.

After mounting, all distances between the components were measured with a ruler ensuring a rough alignment with precision in the order of a few millimeters. The first optical alignment was done without the target due to its low transmittance. The beam from an optical fiber is collimated by an adding a lens and passes on the designated beam height through the middle of the glass window. At a far distance, the position of the beam is marked before the objective is screwed into its holder on top of the two stages. By adjusting them, the marked position of the light beam must remain

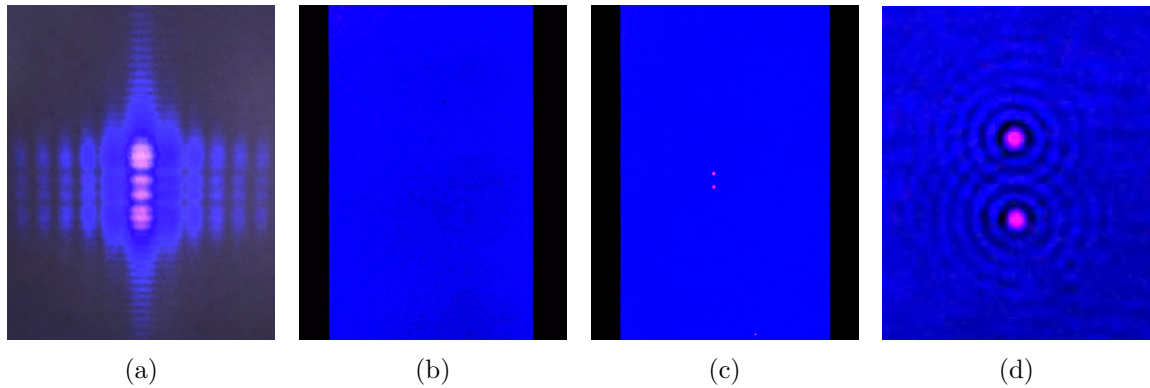


Figure 5.3: Camera view of the target during alignment. First, a blurred spot appears (a). During alignment, a sharp rectangle emerges (b) with the pores in the middle (c). The pores have an Airy disk structure (d).

the same at a far distance. If this is achieved, the focusing lens is positioned in a way that the beam passes through the middle. Again, the path of the light has to remain unchanged. If the lens is placed correctly, the position of the camera has to be arranged. The beam should again hit the camera in the center of the sensor. Now, the target can be inserted at its intended position in front of the other components.

At first, only the semi-transparent membrane is visible on the camera as a bright blurred spot, depicted in Fig. 5.3a. When correcting the distance of the camera to the last lens, the image sharpens and shows a bright rectangle (5.3b). The position on the camera can be adjusted by moving the target with the 3-axis linear translation stage along the x- and y-direction to center the membrane on the camera. Next, the focus has to be found by moving the target along the z-direction, so towards or away from the objective. After a more precise adjustment of the focus, the two nanopores in the middle of the membrane appear as two bright spots, visible in Fig. 5.3c. In 5.3d, the pores are shown enlarged. They exhibit an Airy disk structure, as explained in 3.2. The one-axis stage of the objective is used to align the z-axis much more precisely due to the smaller step size of the picomotor controller. The distance between target and objective is a crucial parameter and has to be adjusted carefully since the depth of field is in a range of less than a micrometer.

For the exact alignment, the picture of the pores has to be evaluated. The intensity of the illuminating light is chosen in a way that the camera is not saturated at the maximum of the Airy Disk peak. There is always a nonzero background since the pores are surrounded by a semitransparent membrane. The intensity of the first minimum of the Airy Disk pattern is below this background due to destructive interference. If

the pores appear elliptical on the camera, the focusing lens has to be adjusted. For comatic aberration (see 3.3), the diffraction disc is not symmetric and exhibits a tail in one direction that resembles a comet. This occurs if the surfaces of the objective are not perpendicular to the z-axis and can be solved by aligning the tilt of the objective in the direction of the tail. If the side maxima of the Airy Disk look brighter on one side than on the other, the target should be moved linearly in that direction. Once there is a good-looking spot found, the target can be shifted around in the x-y-plane. If the focus changes, which means the Airy Disk looks more blurred in some areas, the tilt angle of the objective should be arranged again. This can be done by the four-axis stage of the objective.

In the experiment, the atoms can not be moved like the target in the test setup. Therefore, the position of the objective itself has to be shifted. The available space limits also the range of movement for the objective and the stages. In the test setup, the target is mounted on stages with a larger range making it easier to access properties as field of view in the characterization. For the alignment in the experiment, the atomic cloud itself will be used as a target to focus on. The microscope objective should be placed centered above the upper viewport without any tilt angle between the lens surface and the viewport and perpendicular to the imaging beam. For the mounting procedure, mechanical spacers can help with positioning as it will be further explained in 6.1. With a vertical reference beam and pinholes above and below the objective, the orientation of the objective can be controlled further. The alignment in the main experiment was not fully done when finishing this thesis. The current status and further plans will be explained in Chapter 7. When the atomic cloud is visible on the camera, aberrations and asymmetric behavior can be minimized by the same steps as in the test setup.

5.3 Measurements with a commercial Objective

To test the alignment procedure and check the functionality of the setup, the first measurements were carried out with a commercial microscope objective¹¹. It has a numerical aperture of 0.28, a working distance of 30.6 mm (including a glass plate of 3.5 mm thickness), and a focal length of 10 mm. The dimensions of this objective can be found in the technical drawing in the Appendix A.4. To focus on the camera, a

¹¹Mitutoyo G Plan Apo 20X, Model Number 378-847

lens with focal length $f_{lens} = 200$ mm and 25.4 mm diameter was used, so that the magnification calculates with equation 4.2 to $M = 20$. By determining the known distance between the pores on the camera, the magnification was calculated to be $M = 19.3$. This value was used for the evaluation of the data. The other elements of the test setup were the same as already described, positioned at the respective distances to each other, taking into account the characteristic lengths of the objective. Therefore, the distance between the resolution target and the objective front surface corresponds to the working distance, while the distance between the lens and camera corresponds to its focal length. The focusing lens was placed on a rigid mount without a stage for this first measurements. However, manual alignment of the focusing lens happened to be quite difficult due to the sensitivity of the system, so we decided to place the focusing lens on the five-axis stage for the measurements with the custom-designed objective.

With this arrangement, the alignment was realized with the described procedure by using a wavelength of 405 nm. From the Rayleigh criterion, the minimal radius of the point spread function for this objective calculates to $0.88 \mu\text{m}$. Within the measurements, the best achieved value was $0.95 \mu\text{m}$. This value was determined by the distance between the global maximum and the first minimum of the fit. In Figure 5.4a and 5.4b, the 2D camera image of one nanopore, as well as its 1D cross-section, are depicted with a pixel size of $3.45 \mu\text{m}$ and a magnification of 19.3. The expected Airy Disk shape is visible in both plots, consisting of a main peak and several smaller side maxima, where the intensity is normalized to the maximal value. As previously mentioned, the data has a non-zero background due to the semi-transparent membrane of the resolution target.

When moving the pores out of focus, so in z-direction along the optical axis, the point spread function gets blurred. This was tested by shifting the pores and taking pictures at different distances to the focal plane. The PSF radius values get linearly larger when shifting further, as can be seen in Figure 5.4c.

This was expected from the defocus simulations in 3.4. The distance to the focal plane in which the minimal PSF resolution was still observed is the depth of field, as explained in 4.8. This value was expected to be $1.85 \mu\text{m}$, while $1.6 \mu\text{m}$ was observed in the measurements. To get an idea of how the resolution behaves spatially, the target was moved with the three-axis linear translation stage in the focal plane so perpendicular to the optical axis. Pictures were taken at several points across the area and the PSF radius was calculated from the fit for each data point separately. The results of this are depicted in Figure 5.4d and show the distribution of the values

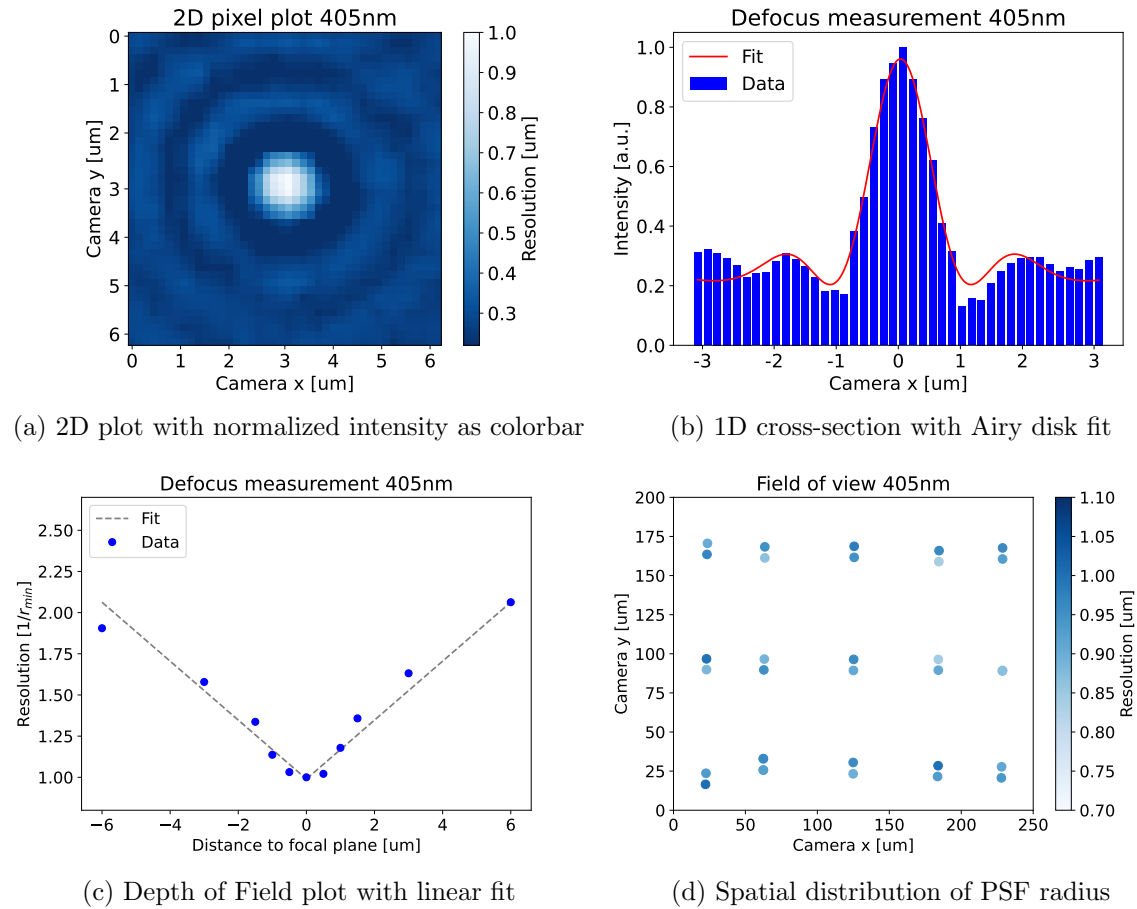


Figure 5.4: Commercial Objective Measurement Plots with a wavelength of 405 nm, a pixel size of $3.45 \mu\text{m}$ and a magnification of $M = 19.3$.

over the camera area. The average of the PSF radius over the area is $1.20 \mu\text{m}$ with a standard deviation of $0.06 \mu\text{m}$. If the tilt angle of the objective is well aligned, the appearance of the pores on the camera changes only slightly when moving them. The PSF radius varies within a small range but the images stay symmetric. The results of the test setup are summarized in Table 5.1. With this, the functionality of the test setup and its components were observed and the commercial objective was replaced by the custom-designed one.

minimal PSF radius	$0.95 \mu\text{m}$
Depth of field	$1.6 \mu\text{m}$
FOV average PSF radius	$1.20 \mu\text{m}$
FOV standard deviation	$0.06 \mu\text{m}$

Table 5.1: Commercial Objective Measurement Results

5.4 Characterization of the custom-designed Objective

Now, we focus on the custom-designed Special Optics objective and want to systematically evaluate its properties, which range from resolution to field of view and depth of field. Furthermore, the characterization process involves the examination of technical specifications, such as focal length and aberration correction. Each of these parameters contributes to the overall performance of the microscope objective and its suitability for imaging tasks.

The output of optical systems can vary at different wavelengths of light due to optical phenomena including refraction, chromatic aberration, and dispersion, as described before. Therefore, all measurements to determine properties for the characterization, described in the following, are performed at the four designated wavelengths 405 nm, 532 nm, 635 nm, and 1064 nm. By that, performance variations can be identified to ensure that the objective meets the requirements of the various possible applications in the experiment. This also allows us to check if the specifications are fulfilled overall.

5.4.1 Magnification

The magnification of the objective is determined by comparing the observed image size with a known reference. In the test setup, a known size is the distance of the two pores on the target, which is $7\ \mu\text{m}$. By measuring the distance of the pores within the captured camera image in pixels and taking into account the known pixel size, the magnification can be extracted. To measure this helps to confirm that the objective is providing the expected level of magnification, which can be calculated with equation 4.2 to $M = 22.87$. The calibration of the objective ensures that the following measurements it are accurate, since the magnification is also needed to determine other observables like resolution and field of view. By calibrating the distance of the pores, a magnification of 24.15 was found for the 405 nm measurements, 22.18 for 532 nm, 25.63 nm for 635 nm, and 20.42 for 1064 nm, respectively. The values vary due to the chromatic focal shift (see 4.10 and 5.4.7). The focal lengths changes for different wavelengths and the positioning of the components was slightly adjusted. The alignment procedure was repeated and the magnification was determined again after changing the wavelength. The magnification measurement contributes to the reliability of the overall characterization, subsequently enabling accurate determinations of other observables within the optical system.

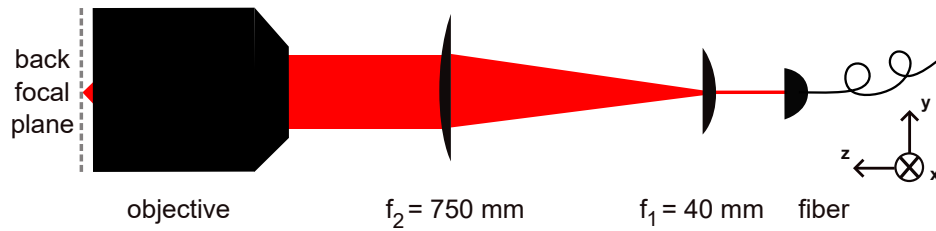


Figure 5.5: Back focus test setup scheme. On the right, a collimated laser beam with a small diameter is provided from an optical fiber. A Keplerian telescope magnifies the beam before it passes the objective, depicted on the left. The back focal plane, where the parallel beams are focused, lies close to the last lens surface of the objective.

5.4.2 Back Focal Plane

The back focus of an objective lens refers to the plane where the light rays that have passed through the objective parallel to the optical axis, converge (see 4.6). This plane is often located inside the objective housing, which makes it inaccessible. For this microscope objective, it lies outside, so behind the surface of the last lens. Hence, the back focus area can be used for light manipulation. For example, a point mirror can be mounted there to reflect the collimated 3D-MOT beam that passes the objective.

The distance from the rear lens element of the objective to the back focal plane is called back focal length. To determine this position, a measurement was conducted in an adapted version of the test setup. Therefore, a large beam had to pass the objective to observe the plane where the rays converge. The optical path is depicted in Figure 5.5. The collimated beam of a 626 nm laser diode is enlarged by a Keplerian beam expander. It consists of two positive lenses, separated by a distance equal to the sum of their focal lengths. The amount of expansion achieved is determined by the focal lengths of the lenses. The magnification calculates to $M = \frac{f_2}{f_1}$, where f_1 is the focal length of the first lens and f_2 corresponds to the second lens in the setup along the beam propagation direction. Therefore, to enlarge the beam f_2 has to be larger than f_1 . For the setup, values of $f_1 = 40$ mm and $f_2 = 750$ mm are chosen leading to a magnification of $M = 18.75$. Thereby, the incoming beam with a diameter of 2 mm is expanded to a diameter of 37.50 mm before passing the objective.

The measurement revealed that the focus lies very close to the surface of the lens of the objective and that the beam diverges very fast afterwards. As depicted in the datasheet (see Appendix A.1), the surface of the last lens lies 1.42 mm inside the housing. When pressing a piece of paper directly on the metal of the holder, the focus appears as a

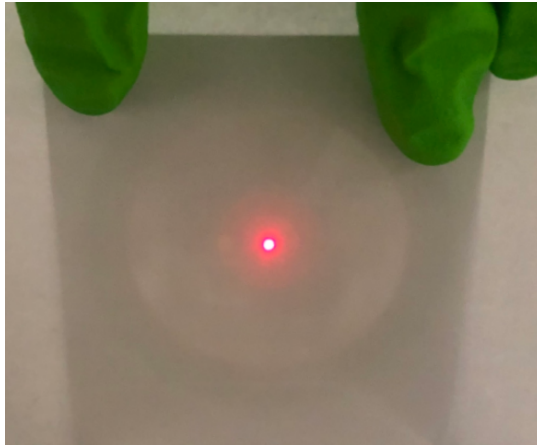


Figure 5.6: The focused red beam behind the objective is visible on a paper that was pressed directly against the mount.

small spot with a size in the order of 1 mm, which is shown in Figure 5.6. The point mirror that should reflect the MOT-beam has to be fixed as close to the surface of the lens as possible. Since the objective itself is fixed in a threaded tube, a second thread can be added from the other side to screw a holder with the point mirror in. The size of the mirror should be around 1mm to reflect the converged beam, while blocking the imaging beam as little as possible.

5.4.3 Resolution

The resolution of an optical system is the ability to distinguish two closely spaced point sources as separate entities rather than a single blurred spot, as explained in Section 3.2. The resolving power of the objective is evaluated by observing the size of the above-described target. For each of the two pores, the point spread function resembles an Airy disk, as can be seen in Figure 5.7. The size of the central spot is related to the resolution of the optical system. Additionally, there are interference effects between the light of the two pores since their point spread functions are partly overlapping. To evaluate this, one can look at the images as well as 1D cross sections in Figure 5.7. The pictures always show a non-zero background. As previously mentioned, this originates in the semitransparent membrane around the pores. The minima of the Airy Disk can have intensity values below the background value due to destructive interference. To determine the size of the main peak, there are two possibilities. It can be calculated as

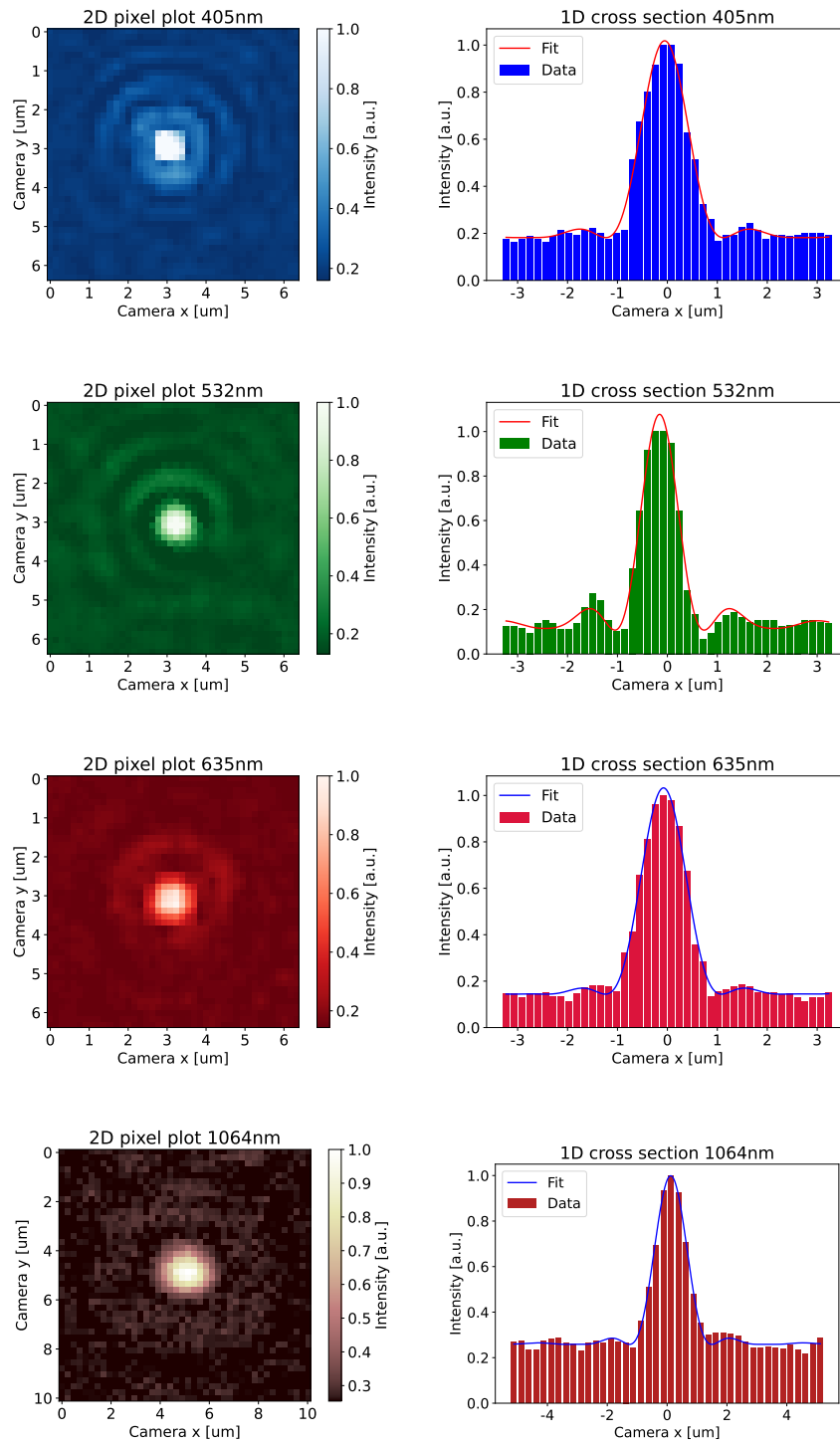


Figure 5.7: Resolution measurement results with the four different wavelengths. In the left column, a section of the camera image is depicted where the colorbar represents the normalized intensity. On the right, a 1D cross-section through the middle with an Airy Disk fit. The pixel size is $5.5\mu\text{m}$ for 1064 nm and $3.45\mu\text{m}$ for the other wavelengths, the scales for x and y extension includes the magnification.

Wavelength	r_{exp}	r_{theo}	DOF_{exp}	DOF_{theo}
405 nm	483 nm	428 nm	$0.3 \mu\text{m}$	$0.467 \mu\text{m}$
532 nm	573 nm	541 nm	$0.4 \mu\text{m}$	$0.591 \mu\text{m}$
635 nm	680 nm	636 nm	$0.5 \mu\text{m}$	$0.695 \mu\text{m}$
1064 nm	1093 nm	1082 nm	$0.9 \mu\text{m}$	$1.181 \mu\text{m}$

Table 5.2: Measurement results for Resolution and Depth of Field, compared with the expected values from theoretical calculations.

the distance between the global maximum and the first minimum of the Airy Disk or as the full width half maximum of the main peak. Those values can be determined from the fits of the cross-section plots depicted in the right column of Figure 5.7. In Table 5.2, the values from the data fit can then be compared to the theoretically calculated ones. Here, the distance between the global maximum and the first minimum was used.

5.4.4 Depth of Field

As explained in Section 4.8, the depth of field is the range of distances in front of and behind the focal plane where objects appear reasonably in focus on the imaging sensor. To measure this, the target is first brought into the focus. By the one-axis linear translation stage, the objective is then moved in z -direction, towards and away from the target. In this way, the distance between the objective lens and the target gets smaller/larger and moves out of the focus area. This can be seen best in the fit based on the image. By plotting the size of the main peak versus the shift in z -direction, the behavior of the defocus can be depicted, where $z = 0$ refers to the focus plane (Fig. 5.8). As described in Section 3.4, the defocus behavior should be linear in first-order approximation. The point spread function gets larger linearly with the distance, as it can be seen in the fits in Figure 5.8. Compared to the theoretical prediction, the values for the PSF radius are slightly larger in the predicted region of the depth of field, calculated in 4.8. The distances to the focal plane in which the minimal PSF radius was still preserved are given in Table 5.2. For 405 nm, the objective can be moved $0.3 \mu\text{m}$ back and forth without affecting the PSF radius. For values up to around $2 \mu\text{m}$, the pores are still resolvable with a radius up to 1.5 times larger than at the focal plane. With larger shifts of several micrometers, the pores appear very blurred and start to overlap until they are not distinguishable anymore.

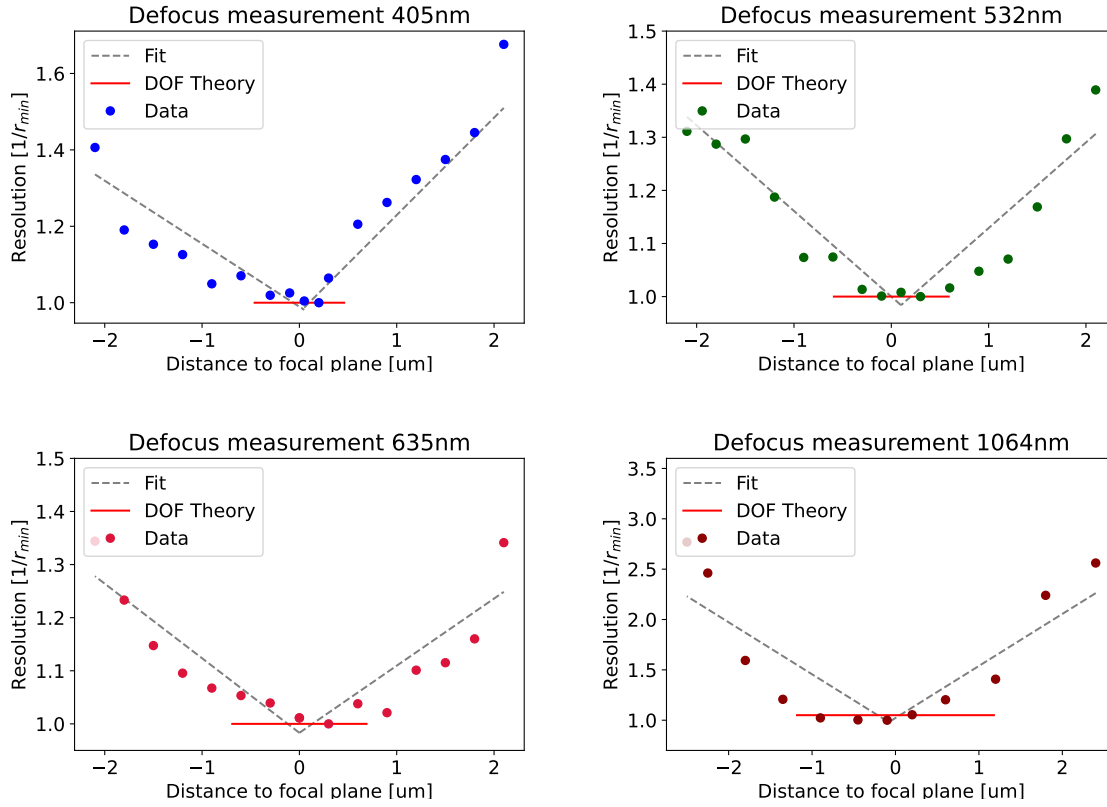


Figure 5.8: Depth of field Measurement Results with the four different wavelength. The dots indicate measured data, the dashed lines are fits. The red lines show the theoretical depth of field range.

5.4.5 Field of View

Following Section 4.9, the field of view is the area in the focal plane where the given parameters of the characterization are fulfilled. Positions outside of the field of view can still be imaged but will be less precise. To visualize this on the camera, the target is moved in the x-y-plane perpendicular to the optical axis with the three-axis linear translation stage. The circular-shaped field of view of the objective was designed to have a diameter of $200\ \mu\text{m}$, which corresponds to a diameter of

$$200\ \mu\text{m} \times M = 200\ \mu\text{m} \times 22.87 = 4\,600\ \mu\text{m} \quad (5.1)$$

on the camera after accounting for magnification. The rectangular camera sensor has an area of

$$(1\,440 \times 1\,080)\ \text{pixel} \times 3.45\ \frac{\mu\text{m}}{\text{pixel}} = (4\,968 \times 3\,726)\ \mu\text{m}. \quad (5.2)$$

Wavelength	FOV average	FOV standard deviation	Strehl ratio
405 nm	0.60 μm	0.13 μm	0.845
532 nm	0.63 μm	0.07 μm	0.882
635 nm	0.72 μm	0.06 μm	0.851
1064 nm	1.42 μm	0.28 μm	0.830

Table 5.3: Measurement results for Field of View. Given is the PSF radius average and its standard deviation over the area as well as the the Strehl ratio.

Thus, the camera sensor is approximately equivalent to the size of the field of view. Consequently, it should be possible to depict the pores clearly on the whole area of the camera. However, towards the edges of the camera sensor, the pores might exhibit a slightly greater degree of blurriness, leading to a reduction in resolution. Throughout this measurement process, it is important to emphasize that only the target’s movement perpendicular to the optical axis was altered. Other degrees of freedom, such as movement in the z-direction or tilt, remained unchanged. This was done deliberately to ensure that the pores remain positioned within the focal plane and are not shifted out of focus. By restricting the movement to the plane perpendicular to the optical axis, it becomes possible to evaluate the objective’s performance specifically in terms of the width and clarity of the captured field. The results of this measurement are shown in Figure 5.9. The resolution is mostly uniform over the depicted area, as can be seen from the colorbars of the plots representing the PSF radius. However, some single spots appear to have larger values.

By determining the PSF size for every data point of the measurement, the average of the PSF size in the field of view can be calculated. This value, together with its standard deviation, is given in Table 5.3 for the four wavelengths of interest. Following the definition of the field of view over the Strehl ratio, the intensity ratio between the actual and the ideal system has to be calculated (see Section 3.3). This was done by looking at the maximal value of the intensity, which corresponds to the height of the main peak. The radius is linked to the intensity maximum in a way that a larger radius comes with a smaller maximal intensity. This is due to the constant incoming power corresponding to a constant area under the curve. The maximal intensity value was compared between the field of view measurements and the single point measurements presented in Section 5.4.3. The deviation between them was lower than 20% on average, which leads to a Strehl ratio of >0.8 . This meets the conditions for the field of view over the observed area. The Strehl ratios for the wavelengths are given in Table 5.3.

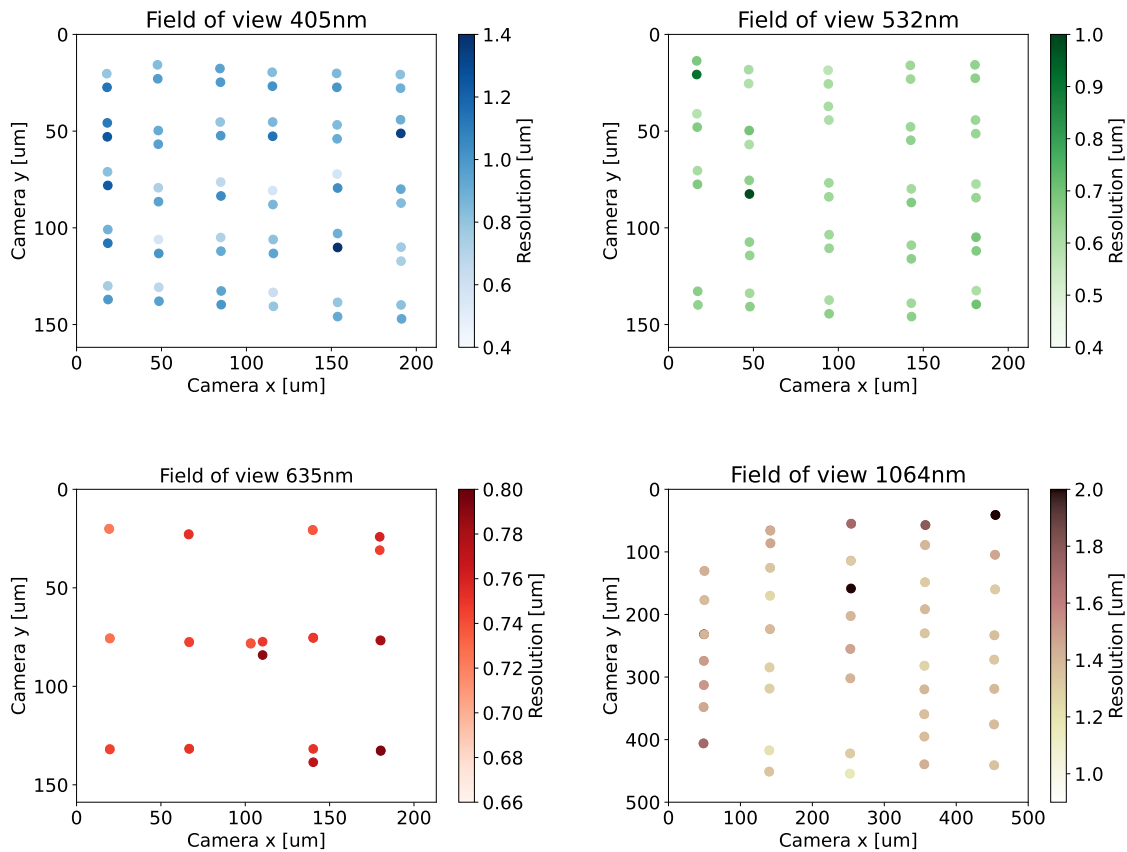


Figure 5.9: Field of View Measurement Results with the four different wavelengths. The dots indicate measured data, while the color bar presents the PSF radius in micrometers.

5.4.6 Aberrations and Tilt

As already described in Section 3.3, various aberrations can occur that cause deviations from an ideal image formation. They can result in distortion, blurring, and other image quality issues. First of all, the surfaces of all optical elements have to be clean. Dust particles on the lens surfaces can scatter and diffract light, leading to reduced resolution and the formation of speckles when used with coherent light. To prevent this during the time the setup was installed, the lenses, as well as the camera sensor were covered to prevent dust from settling on the surfaces whenever no measurement was running. The microscope objective itself was already designed to minimize several aberrations through the use of complex lens systems, coatings, and other techniques described in Section 4.10. However, it's still a challenge to eliminate all aberrations completely in the optical path of the setup. Spherical aberrations and coma can be prevented by precise alignment. An important degree of freedom for this is the tilt angle between

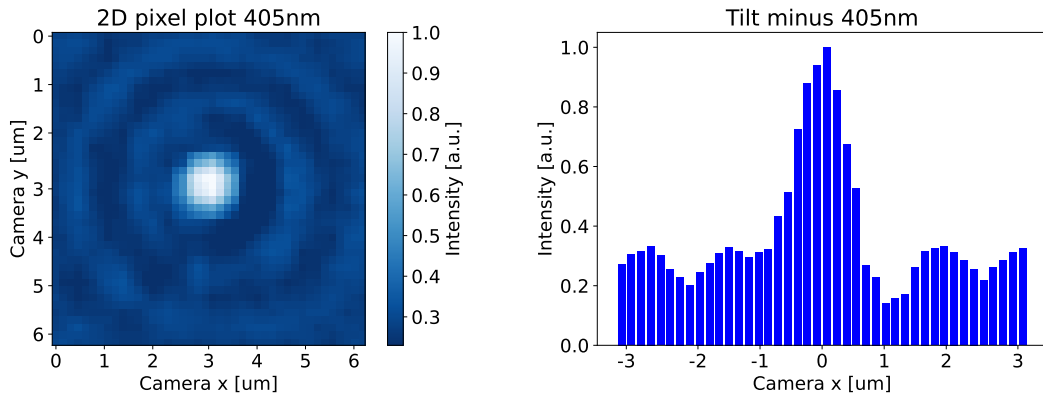


Figure 5.10: Measurements with tilt-shift. On the left, the 2D pixel plot is shown where the central peak is shifted. On the right, the 1D cross-section is plotted. The first minimum on the left of the main peak is shallower, and the one on the right is deeper, respectively. The objective was tilted in the x-direction by 5.72 mrad.

the objective and the glass window. It can be controlled by the tilt stage, where the objective is mounted on. Since the glass window and the target are fixed without any rotational degree of freedom, the objective surface tilts simultaneously to both of them. In the measurements, the effect of the tilt can be best seen in the 1D cross sections. The first minimum next to the main peak appears shallower on one side but deeper on the other. This leads to an asymmetric shape, as can be seen in Figure 5.10 with a tilt in the x-direction by 5.73 mrad. In the 2D pixel plot, shown on the left of, the central spot of the Airy Disk shape is not positioned in the middle of the interference rings but shifted to the left. Therefore, the first side maximum on the left is closer, leading to a stronger pronounced minimum on the right, as visible in the 1D cross-section on the right.

5.4.7 Chromatic Focal Shift

As written in Section 4.10, the chromatic focal shift is an important feature of this setup. It is set to be smaller than $10\ \mu\text{m}$ in the wavelength range of interest. This was experimentally checked by exchanging the incoming wavelength while keeping all other devices in place. Thereby, it was possible to observe if and how the focus changes. After the replacement of the laser diode, the point spread function looked blurred. By moving the objective along the z-direction with the one-axis linear translation stage, the image was recovered. The number of steps needed to come back to the initial state

Wavelength	T_{exp}	T_{theo}
405 nm	0.79	> 0.78
532 nm	0.88	> 0.86
635 nm	0.91	> 0.86
1064 nm	0.93	> 0.86

Table 5.4: Measured transmission coefficients for the four wavelengths and the theoretical values provided by Special Optics.

when exchanging the wavelengths could be read directly from the control panel. The stepsize brings an uncertainty, since the stage is open loop, as explained in 5.1. It depends on load and direction, due to the difference in expansion and contraction of the piezo stack. Taking this into account, the focal shift was specified to be $19.5 \mu\text{m}$ with an error of $2 \mu\text{m}$ when exchanging between 405 nm and 532 nm wavelength. This was observed for exchanging them in both direction, so from 405 nm to 532 nm and vice versa. From the theoretical considerations (Figure 4.3) it appears that the focal shift between those wavelengths should rather be around $1 \mu\text{m}$. However, the optical system contains besides the objective also the focusing lens. Their focal plane shows as well chromatic focus shift larger than the one of the objective. Therefore, the lens is probably the main reason for the unexpected large value. The company Thorlabs provides the diffraction index for the material of the lens¹² that varies for different wavelengths. From the lensmaker equation, one can then calculate the focal length for each of the wavelengths and, from the difference between them, the chromatic focal shift. Between 405 nm and 532 nm, the difference calculated from the change in diffraction index is $17.53 \mu\text{m}$. Subtracting this from the measuring result of $19.5 \mu\text{m}$ leads to a value of about $2 \mu\text{m}$. Since this also the size of the error, one can not directly conclude to the focal shift from the objective. Therefore, the measurement can only provide an upper limit of the observable due to the experimental restrictions of the setup and the imperfections of the other elements.

5.4.8 Transmission

As described in Section 4.11, the transmission of the objective lens is optimized by choosing a coating that minimizes reflections at the four specific wavelengths of interest. To quantify this behavior, a beam with known intensity is sent through the objective. The intensity afterward is measured again by a power meter placed behind the objective

¹²Thorlabs N-BK7 Plano-Convex Lens LA1727-AB ($f = 750 \text{ mm}$)

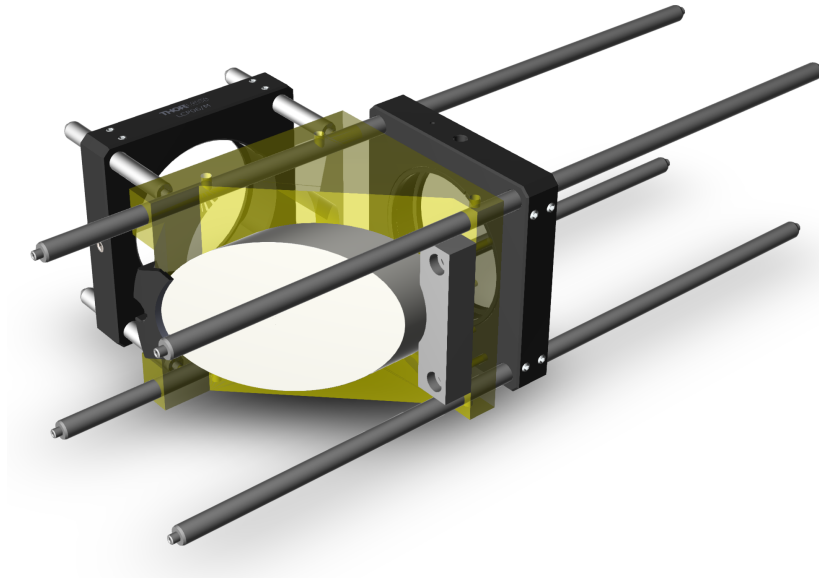


Figure 5.11: Dichroic mirror in its mount, consisting of a main piece and two side parts, providing the only contact to the mirror surface. Figure taken from [54].

in the focal plane. In Table 5.4, the measured transmission coefficients for the different wavelengths are shown. These are measured without an angle of incident. So the light passed the lens perpendicular to the surface. Notably, as the wavelength decreases, the reflective properties of the material become more pronounced, leading to a decrease in transmission. The coating is selected to minimize reflections at the four specific wavelengths crucial for the experiment, as discussed in 4.11. It has to be noticed that in the tests a slightly smaller wavelength of 405 nm is used compared to the 421 nm employed in the experiment. Consequently, the value presented in the table for 405 nm serves only as a lower boundary for the behavior at 421 nm. Another factor that has an impact on the transmission is the angle of incidence of the light. When changing the angle to non-zero values, a slightly different transmission was observed. This was predicted from theoretical simulations, as can be seen in Fig. 4.4 for an angle of 41° .

5.4.9 Imaging Setup including a Dichroic Mirror

In the experiment, we want to combine the imaging with the DMD setup (see 6.1). They work with wavelengths of 421 nm and 532 nm, which both have to pass the microscope objective. Therefore, it is useful to have a dichroic mirror to separate or mix light

points with the mirror surface in order to minimize external stress. Mirror and mount are shown in Figure 5.11 inside of a cage system. Still, the surface is slightly stressed, which leads to small distortions of the surface near the contact points on the mirror. Therefore, it is crucial to hit the surface with the laser beam far away from the edges, ideally in the middle. To test this spatial behavior, an additional mirror was added to the optical path before and behind the dichroic mirror, respectively. The first mirror controls the position on the dichroic and the second one ensured that the light would still hit the camera sensor afterward.

Test measurements were performed with a wavelength of 405 nm. It was observed that the distortions of the mirror have a strong impact on the quality of the point spread function and on interference effects. This occurred mainly if the mirror was hit by the beam rather on the side and is depicted in Figure 5.12. When the light is reflected at a position close to the side, where the mount touches the mirror surface, the point spread function is strongly affected. As visible in Figure 5.12a, it differs a lot from the expected Airy Disk that was observed before in the setup without the dichroic. When shifting the beam away from the side closer to the center, the distortion gets smaller and the Airy Disk shape recovers. Still, the shape of the point spread function appears rather elliptical than circular, and the main peak has a larger radius, as depicted in Figure 5.12b. On the other hand, when the mirror gets hit in the center, the point spread function has again the expected Airy Disk shape with a similar radius as observed before. This can be seen in Figure 5.12c. Note that a detailed examination of the impact of the mirror surface on the wavefront was performed beforehand and can be found in [54].

6 Implementation

The microscope objective must seamlessly integrate into the overall apparatus while ensuring stability, alignability, and ease of operation. It is placed very close on top of the upper inverted viewport, between the coils. Therefore, the objective and holder have to be made out of non-magnetic materials. Also, the dimension of the objective is limited by the given space. The imaging beam will enter the science chamber from below, through the lower viewport. One challenge was to ensure translational and rotational degrees of freedom for positioning and centering the objective. This is crucial to align the imaging system. However, it should be rigid enough to be unaffected by external vibrations.

6.1 Final Assembly

Above the main chamber, an additional breadboard is placed on several posts with 300 mm vertical space to the lower one. It has a hole directly above the chamber to let the imaging beam pass. Next to it, the mount of the objective has to be attached. A right-angle adapter plate connects the upper breadboard with the one-axis translation stage that was already used in the test setup. It has a small step size to enable precise adjustment of the focal plane and moves vertically along the optical axis. The latter is different from the reference system in the test setup, where the optical axis was placed horizontally. On the one-axis stage, an adapter plate is screwed, which enables the mounting of the four-axis stage. It translates along and rotates around the x - and y -axis and enables to align the horizontal position and tilt angle. Both stages can be remotely controlled by a micro-controller. The objective is screwed into a threaded tube, which itself is fixed on the four-axis stage. To ensure that the objective will not hit the viewport and damage one of them, spacers have been added to the assembly, designed by Joschka Schöner. These small elements are screwed onto the main chamber and provide a mechanical barrier preventing the objective to move down further than intended. This was in particular useful for the first alignment

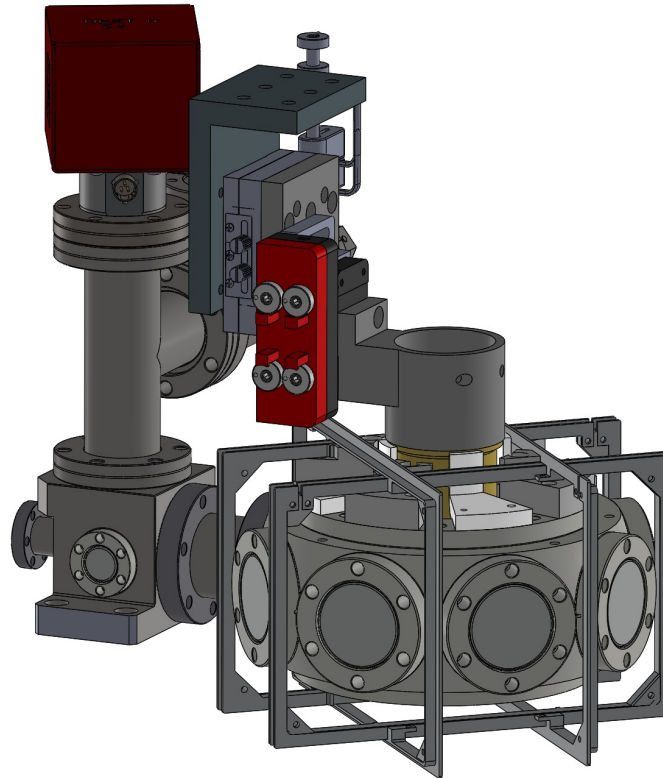


Figure 6.1: Final assembly for the implementation into the main experiment. The objective is placed between the coils directly above the upper viewport of the science chamber. It is screwed into a tube, which is mounted on the 4-axis stage that is connected to the 1-axis stage via an adapter plate. The 1-axis stage is screwed onto an angle plate. The white spacers ensure a minimal distance of 1 mm between the objective and the viewport.

procedure. By careful observation of the distance between each of the spacers, the linear and angular orientation of the objective was adjusted. The full assembly is depicted in Figure 6.1. The design was mainly created by Shuwei Jin. On top of the upper breadboard, a lens system is mounted to focus on the low-noise qCMOS camera¹. The choice of the focal lengths and the resulting magnification will be discussed in 6.2.

This mechanical assembly is the basis for the vertical imaging setup that will be described next. The imaging beam with a wavelength of 421 nm hits the atomic cloud from below and crosses the objective afterward. It is reflected by a mirror mounted on the upper breadboard after passing through the hole, crosses the following lenses, and hits the imaging camera at a beam height of 55 mm. The focus plane of the last lens

¹Hamamatsu ORCA-Quest qCMOS camera C15550-20UP

lies at the camera surface. In its final imaging position, the foremost surface of the objective is positioned 2 mm above the upper viewport of the main chamber (see 4.2).

Because of its position directly above the viewport, one of the MOT beams has to cross the microscope objective. Therefore, the MOT beam coming from below will be reflected by a point mirror, sputtered on a waveplate. It is mounted at the back focus of the objective, which is outside of the housing but very close to the surface of the last lens. Therefore, the waveplate can be mounted within an additional thread in the same tube as the objective. With this point-like aluminum mirror in the middle, it can reflect the MOT-beam without taking away much intensity from the imaging.

Inclusion of the DMD setup As already mentioned in 2.3 and 5.4.9, the imaging setup will be combined with the DMD setup in the experiment. While the imaging beam has a wavelength of 421 nm, the DMD system will use a 532 nm beam. Both beams have to pass the microscope objective. To make this possible, a dichroic mirror, which reflects 421 nm and transmits all wavelengths above 532 nm, is mounted above the objective. The 421 nm beam passes the objective from below and will be reflected by the dichroic mirror onto the following lens. The 532 nm beam will illuminate the DMD, which modulates its intensity profile. Afterward, it gets transmitted by the dichroic mirror and passes the objective from above to project a potential onto the atoms. The DMD setup is further discussed in [40].

6.2 Magnification

By choosing the focal length of the lens after the objective, the magnification M of the imaging system is determined. A larger magnification leads to more details in the image but comes along with a smaller effective sensor size. Following the Nyquist-Shannon sampling theorem, the PSF of the smallest resolvable feature must be sampled by a minimum of 2 pixels across its radius [55]. Therefore, the magnification should have at least a value of $M = \frac{2d_{px}}{r_{min}}$, with a known pixel size of $d_{px} = 4.6 \mu\text{m}$. Since the minimal PSF radius of the system is around 500 nm, a magnification of about $M \approx 20$ is needed to be able to resolve the smallest possible points on the camera. For the 4096×2304 pixels on the camera, the effective sensor size would then be $942 \times 530 \mu\text{m}$. Since a smaller magnification comes with a larger effective sensor size, it is favorable for the first alignment steps.

With a focal lens of $f_1 = 400$ mm, the magnification of the setup calculates to

$$M_1 = \frac{f_1}{f_{\text{objective}}} = \frac{400 \text{ mm}}{32.8 \text{ mm}} \approx 12.20. \quad (6.1)$$

To be able to vary the magnification, two additional lenses in a telescope setup are added behind. This allows to use the imaging system for different requirements. With the focal lengths $f_2 = 500$ mm and $f_3 = 300$ mm, a further magnification factor of

$$M_2 = \frac{f_2}{f_3} = \frac{300 \text{ mm}}{500 \text{ mm}} = 0.6 \quad \text{or} \quad M_3 = \frac{f_3}{f_2} = \frac{500 \text{ mm}}{300 \text{ mm}} = 1.67 \quad (6.2)$$

can be achieved, depending on the arrangement. If the lens with the smaller focal length is put first in the optical path, followed by the larger one, an overall magnification of

$$M_1 \times M_2 = 12.20 \times 0.6 = 7.32 \quad (6.3)$$

is reached. For the inverse order, so placing first the lens with the larger focal lens followed by the smaller one, the value calculates to

$$M_1 \times M_3 = 12.20 \times 1.67 = 20.37. \quad (6.4)$$

Meanwhile, the position and alignment of the previous elements of the setup remain unchanged. This means the objective and the focusing lens do not need to be modified. The different magnifications can be used to access various situations in the experiment and provide a broader platform for the functionality of the imaging setup. In the focus of the last lens, the low-noise qCMOS camera is placed.

7 Summary and Outlook

In this thesis, the characterization of a custom-designed microscope objective for a high-resolution imaging system was presented. The main goal was to check the properties and overall performance of the objective, which was done in a test setup. We discussed the expectations and limitations of the imaging system by running simulations of its optical performance based on theoretical concepts. After testing an alignment procedure for the setup, characterization measurements were carried out to determine the following properties of the optical setup: Most important for the imaging system within the experiment is its resolution at the wavelengths 421 nm and 532 nm. The smallest measured radius of the point spread function was 483 nm at a wavelength of 405 nm and 573 nm at a wavelength of 532 nm. Over the whole field of view, the average PSF radius was $0.60\ \mu\text{m}$ with a standard deviation of $0.13\ \mu\text{m}$ at 421 nm wavelength and $0.63\ \mu\text{m}$ with a standard deviation of $0.07\ \mu\text{m}$ at 532 nm wavelength. We determined a depth of field of $0.3\ \mu\text{m}$ and $0.4\ \mu\text{m}$ at 421 nm and 532 nm, respectively. The chromatic focal shift is smaller than $15\ \mu\text{m}$ over the wavelength range of 405 nm to 1064 nm. The tilt of the objective has some noticeable effect for angles as small as 5 mrad. For 405 nm, a transmission coefficient of 0.78 was measured. For the other wavelengths, namely 532 nm, 626 nm, and 1064 nm, this value was above 0.88. When the dichroic mirror is included in the imaging setup, it should be hit at the center. Since the surface is very sensitive to stress, hitting it on the side leads to distortions of the wavefront. The gained knowledge was used to implement the imaging system into the ultracold atom experiment.

Currently, the objective is mounted on translation stages below the upper breadboard and above the viewport of the main chamber. The lenses and camera were installed as well. The proper alignment of the whole system still has to be done. One approach was to produce quantum droplets to have a small object that can be used for the procedure comparable to the nanopores used in the test setup. This can be done by ramping the scattering length down using an external magnetic field and letting the cloud expand freely. Even though a droplet could be formed, the alignment procedure

based on this idea turned out to be too involved. Another approach is to use optical tweezers created by the objective itself. A laser beam that passes the objective from above is tightly focused on the focal point. When using red-detuned light, the atoms experience an attractive force due to the transfer of momentum from the scattering of the photons and get trapped at the beam waist. This can be used to adjust the spatial position of the objective. For dysprosium, a wavelength of 532 nm can be used to create an attractive force. An incoming beam with a diameter of 4.5 mm leads to a waist diameter of about 1.5 mm. The position of the trapped atoms can then be aligned with the atomic cloud. After the alignment of the objective is done, the implementation of the DMD setup in the main experiment is planned. It was already characterized in an additional test setup [40] and will pass the microscope objective as well. The dichroic mirror connects the optical paths of imaging and DMD setup with their wavelengths of 421 nm and 532 nm, respectively. As soon as the objective is in place, it opens many new possibilities for the experiment.

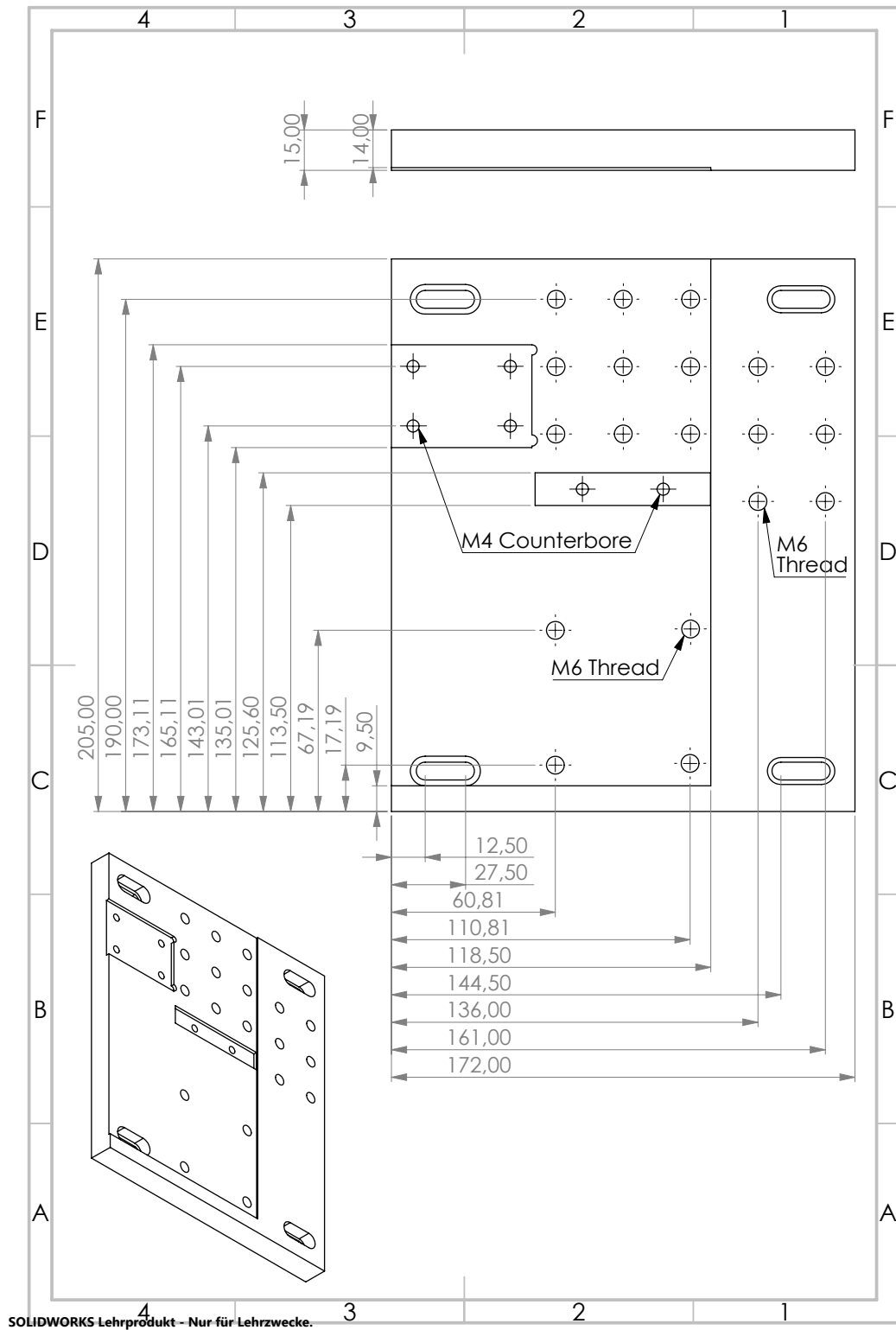


Figure A.2: Drawing of the breadboard for the test setup.

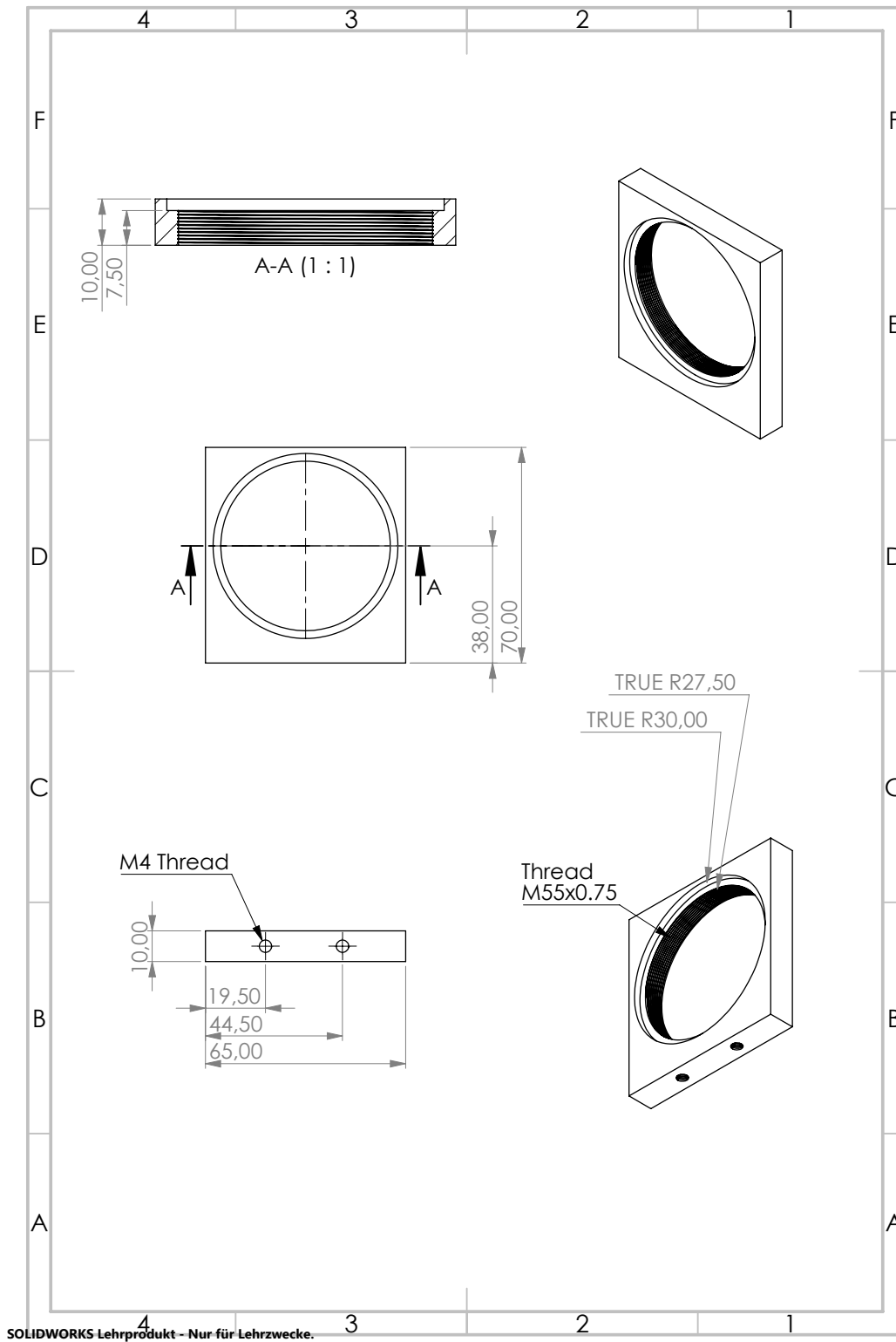
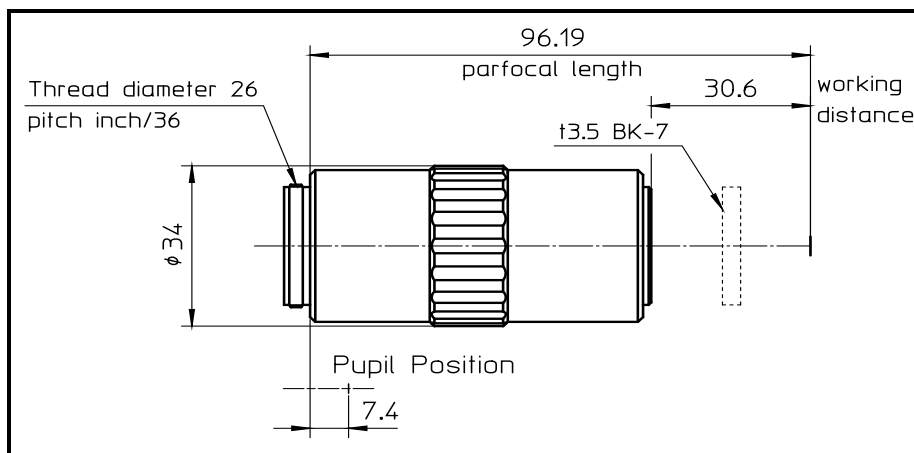
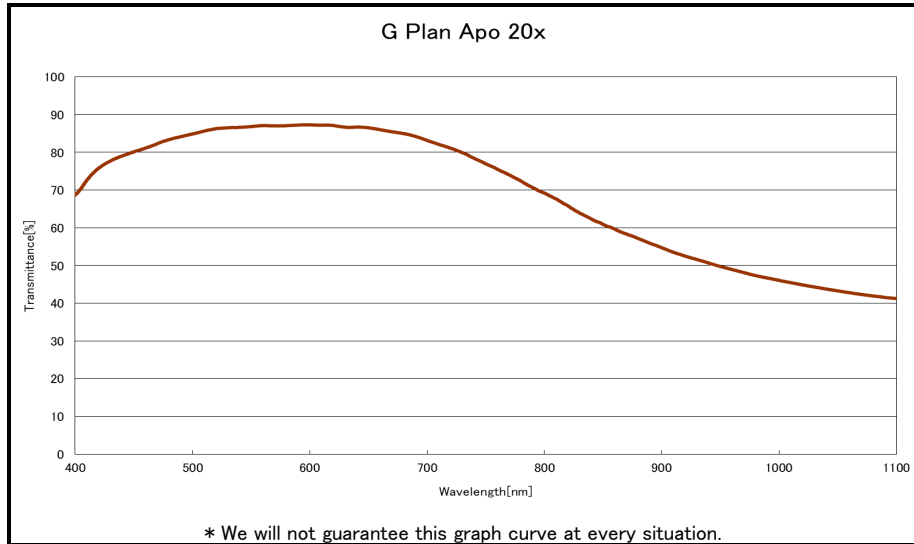


Figure A.3: Drawing of the mount for the objective.

378-847

378847A



focal length :	fd=10mm
numerical aperture :	NA=0.28
exit pupil diameter :	Φ5.6mm
Object size :	Φ1.5mm

Figure A.4: Transmission curve, technical drawing and characteristic lengths of the commercial objective, provided by Mitutoyo.

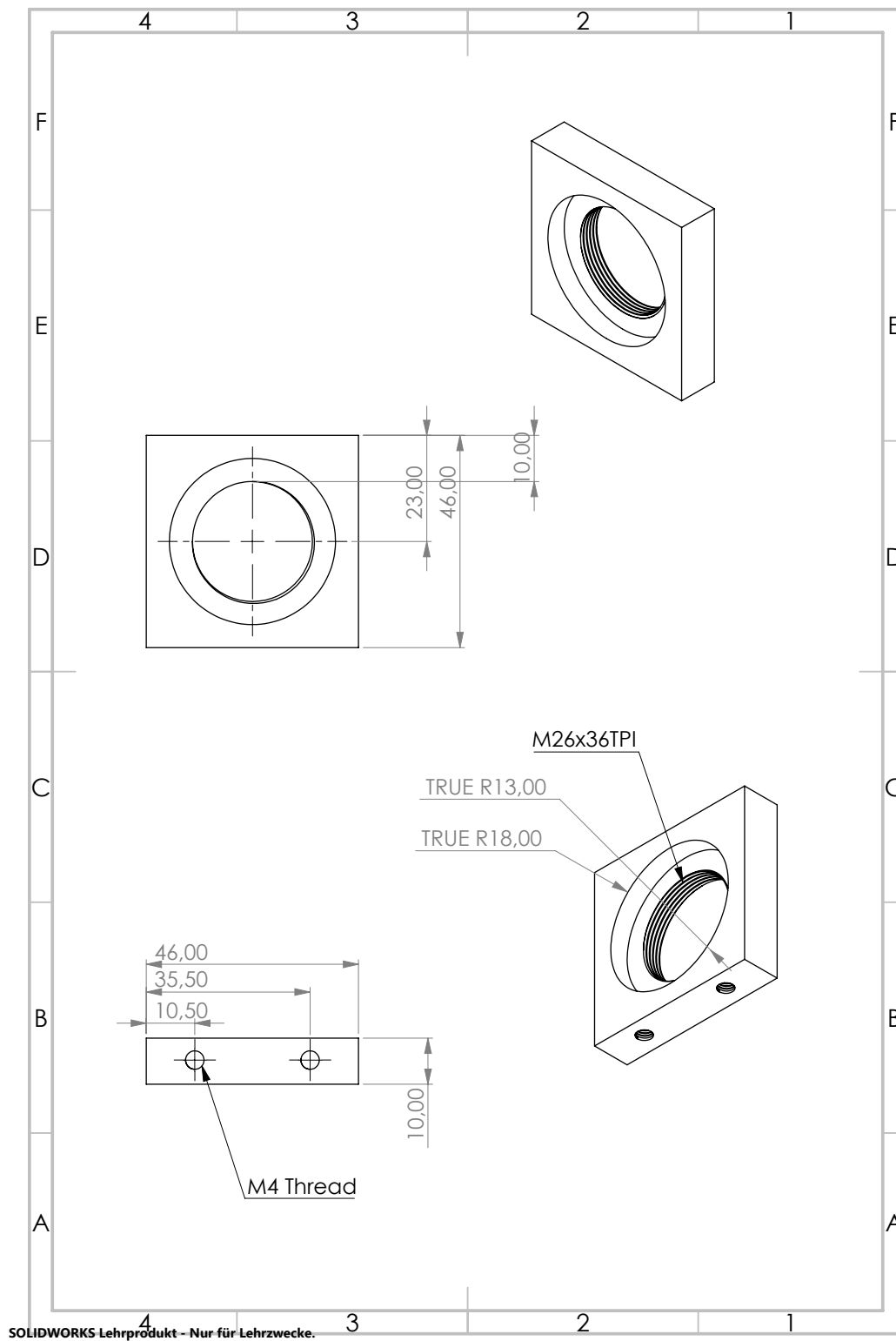


Figure A.5: Drawing of the mount for the Mitutoyo objective.

A.2 Pictures

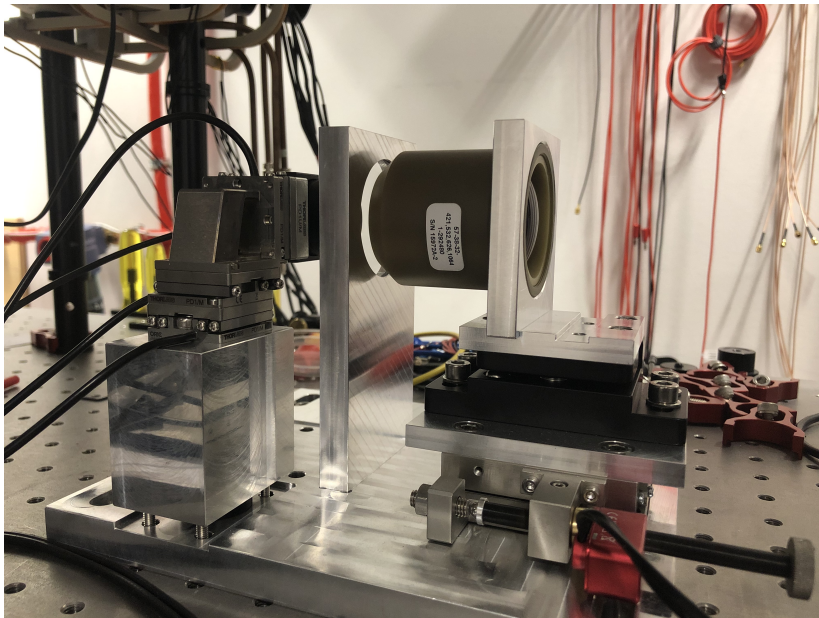
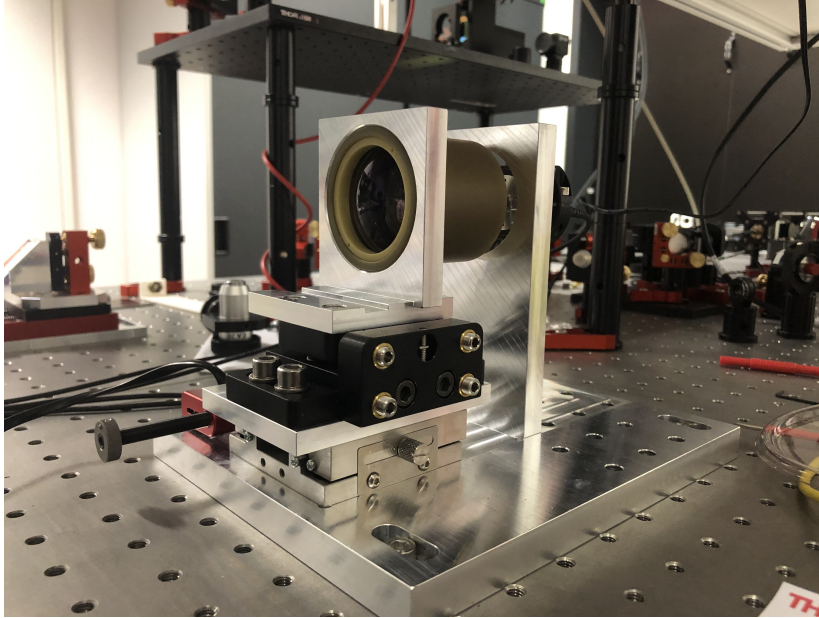


Figure A.7: Breadboard of the test setup in the preparation lab.

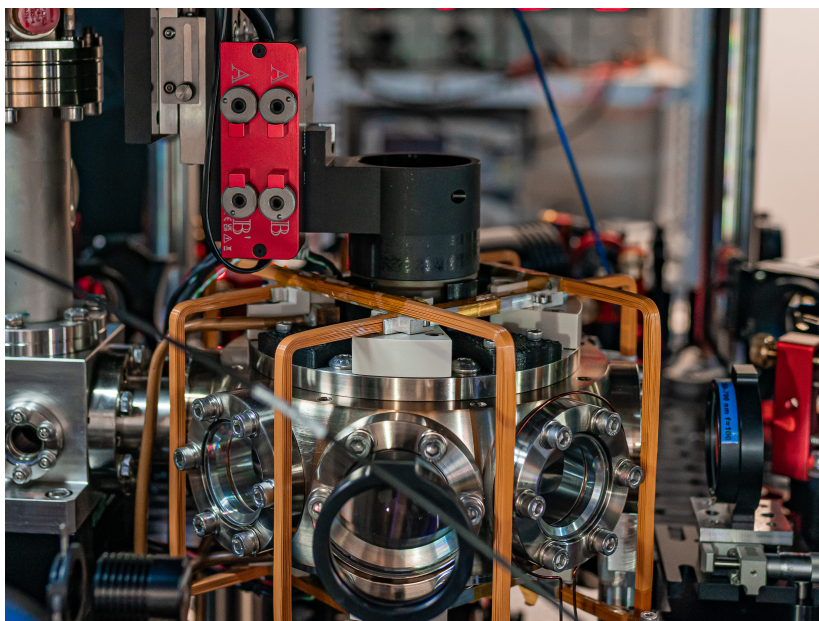
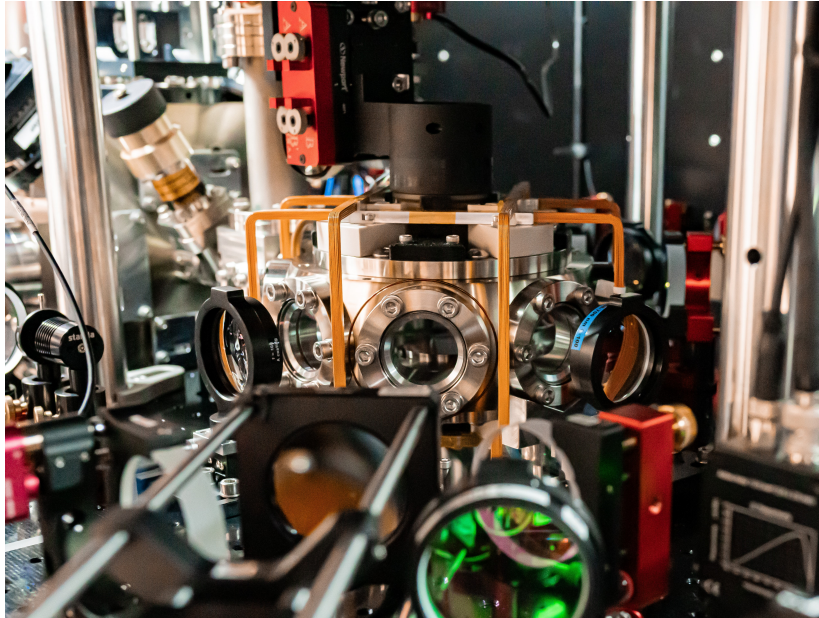


Figure A.8: Assembly in the experiment above the main chamber. Pictures taken by Maurice Rieger.

B Bibliography

- [1] Wolfgang Ketterle. “Nobel lecture: When atoms behave as waves: Bose-Einstein condensation and the atom laser”. In: *Reviews of Modern Physics* 74.4 (2002), p. 1131.
- [2] Wolfgang Ketterle, Dallin S Durfee, and DM Stamper-Kurn. “Making, probing and understanding Bose-Einstein condensates”. In: *arXiv preprint cond-mat/9904034* (1999).
- [3] Immanuel Bloch, Jean Dalibard, and Wilhelm Zwerger. “Many-body physics with ultracold gases”. In: *Rev. Mod. Phys.* 80 (3 July 2008), pp. 885–964. DOI: 10.1103/RevModPhys.80.885.
- [4] Andrew D. Ludlow, Martin M. Boyd, Jun Ye, E. Peik, and P. O. Schmidt. “Optical atomic clocks”. In: *Rev. Mod. Phys.* 87 (2 June 2015), pp. 637–701. DOI: 10.1103/RevModPhys.87.637.
- [5] I. M. Georgescu, S. Ashhab, and Franco Nori. “Quantum simulation”. In: *Rev. Mod. Phys.* 86 (1 Mar. 2014), pp. 153–185. DOI: 10.1103/RevModPhys.86.153.
- [6] Thaddeus D Ladd, Fedor Jelezko, Raymond Laflamme, Yasunobu Nakamura, Christopher Monroe, and Jeremy Lloyd O’Brien. “Quantum computers”. In: *nature* 464.7285 (2010), pp. 45–53.
- [7] Christian Gross and Waseem S Bakr. “Quantum gas microscopy for single atom and spin detection”. In: *Nature Physics* 17.12 (2021), pp. 1316–1323.
- [8] Lauriane Chomaz, Igor Ferrier-Barbut, Francesca Ferlaino, Bruno Laburthe-Tolra, Benjamin L Lev, and Tilman Pfau. “Dipolar physics: A review of experiments with magnetic quantum gases.” In: *Reports on Progress in Physics* (2022).
- [9] William D Phillips. “Nobel Lecture: Laser cooling and trapping of neutral atoms”. In: *Reviews of Modern Physics* 70.3 (1998), p. 721.
- [10] Steven Chu. “Nobel Lecture: The manipulation of neutral particles”. In: *Reviews of Modern Physics* 70.3 (1998), p. 685.

- [11] Claude N Cohen-Tannoudji. “Nobel Lecture: Manipulating atoms with photons”. In: *Reviews of Modern Physics* 70.3 (1998), p. 707.
- [12] Eric A Cornell and Carl E Wieman. “Nobel Lecture: Bose-Einstein condensation in a dilute gas, the first 70 years and some recent experiments”. In: *Reviews of Modern Physics* 74.3 (2002), p. 875.
- [13] Rudolf Grimm, Matthias Weidemüller, and Yurii B Ovchinnikov. “Optical dipole traps for neutral atoms”. In: *Advances in atomic, molecular, and optical physics*. Vol. 42. Elsevier, 2000, pp. 95–170.
- [14] Markus Greiner, Olaf Mandel, Tilman Esslinger, Theodor W Hänsch, and Immanuel Bloch. “Quantum phase transition from a superfluid to a Mott insulator in a gas of ultracold atoms”. In: *nature* 415.6867 (2002), pp. 39–44.
- [15] Zoran Hadzibabic, Peter Krüger, Marc Cheneau, Baptiste Battelier, and Jean Dalibard. “Berezinskii–Kosterlitz–Thouless crossover in a trapped atomic gas”. In: *Nature* 441.7097 (2006), pp. 1118–1121.
- [16] Dale G Fried, Thomas C Killian, Lorenz Willmann, David Landhuis, Stephen C Moss, Daniel Kleppner, and Thomas J Greytak. “Bose-Einstein condensation of atomic hydrogen”. In: *Physical Review Letters* 81.18 (1998), p. 3811.
- [17] Cl C Bradley, CA Sackett, JJ Tollett, and Randall G Hulet. “Evidence of Bose-Einstein condensation in an atomic gas with attractive interactions”. In: *Physical review letters* 75.9 (1995), p. 1687.
- [18] Kendall B Davis, M-O Mewes, Michael R Andrews, Nicolaas J van Druten, Dallin S Durfee, DM Kurn, and Wolfgang Ketterle. “Bose-Einstein condensation in a gas of sodium atoms”. In: *Physical review letters* 75.22 (1995), p. 3969.
- [19] Tino Weber, Jens Herbig, Michael Mark, Hanns-Christoph Nagerl, and Rudolf Grimm. “Bose-Einstein condensation of cesium”. In: *Science* 299.5604 (2003), pp. 232–235.
- [20] Giovanni Modugno, Giacomo Roati, Francesco Riboli, Francesca Ferlaino, Robert J Brecha, and Massimo Inguscio. “Collapse of a degenerate Fermi gas”. In: *Science* 297.5590 (2002), pp. 2240–2243.
- [21] Axel Griesmaier, Jörg Werner, Sven Hensler, Jürgen Stuhler, and Tilman Pfau. “Bose-Einstein condensation of chromium”. In: *Physical Review Letters* 94.16 (2005), p. 160401.

- [22] Mingwu Lu, Nathaniel Q Burdick, Seo Ho Youn, and Benjamin L Lev. “Strongly dipolar Bose-Einstein condensate of dysprosium”. In: *Physical review letters* 107.19 (2011), p. 190401.
- [23] John R. de Laeter, John Karl Böhlke, P. De Bièvre, H. Hidaka, H. S. Peiser, K. J. R. Rosman, and P. D. P. Taylor. “Atomic weights of the elements. Review 2000 (IUPAC Technical Report)”. In: *Pure and Applied Chemistry* 75.6 (2003), pp. 683–800. DOI: doi:10.1351/pac200375060683.
- [24] John Emsley. *Nature’s building blocks: an AZ guide to the elements*. Oxford University Press, USA, 2011.
- [25] Ian Baker. “Rare Earth magnets”. In: *Fifty Materials That Make the World* (2018), pp. 187–194.
- [26] William M Haynes. *CRC handbook of chemistry and physics*. CRC press, 2014.
- [27] Shuwei Jin, Jianshun Gao, Karthik Chandrashekhara, Christian Gölzhäuser, Joschka Schöner, and Lauriane Chomaz. “Two-dimensional magneto-optical trap of dysprosium atoms as a compact source for efficient loading of a narrow-line three-dimensional magneto-optical trap”. In: *Phys. Rev. A* 108 (2 Aug. 2023), p. 023719. DOI: 10.1103/PhysRevA.108.023719.
- [28] P. Ilzhöfer, G. Durastante, A. Patscheider, A. Trautmann, M. J. Mark, and F. Ferlaino. “Two-species five-beam magneto-optical trap for erbium and dysprosium”. In: *Phys. Rev. A* 97 (2 Feb. 2018), p. 023633. DOI: 10.1103/PhysRevA.97.023633.
- [29] William Lunden. “Development of a new Dy quantum gas experiment”. PhD Thesis. Massachusetts Institute of Technology, 2020.
- [30] Gianmaria Durastante. “Creation of Erbium-Dysprosium Dipolar Quantum Mixtures and Their Interspecies Feshbach Resonances”. PhD Thesis. University of Innsbruck, 2020.
- [31] Cheng Chin, Rudolf Grimm, Paul Julienne, and Eite Tiesinga. “Feshbach resonances in ultracold gases”. In: *Rev. Mod. Phys.* 82 (2 Apr. 2010), pp. 1225–1286. DOI: 10.1103/RevModPhys.82.1225.
- [32] Christian Gölzhäuser. “Building a new Dy quantum gas experiment”. Bachelor Thesis. University Heidelberg, 2021.

- [33] Joschka Schöner. “Magnetic-Field Setup for Magneto-Optical-Trapping and Interaction-Tuning in Novel Dysprosium Quantum Gas Experiment”. Master Thesis. University Heidelberg, 2022.
- [34] Lennart Hoenen. “Fast, High Precision Low Noise Bipolar Power Supply for Magnetic Field Coils in Ultra-Cold Dysprosium Experiment”. Bachelor Thesis. University Heidelberg, 2022.
- [35] Jianshun Gao. “A First Two-Dimensional Magneto-Optical Trap for Dysprosium”. Ph.D. admission thesis. University Heidelberg, 2022.
- [36] Paul Holzenkamp. “An Optical Dipole Trap with Tunable Geometry for Dysprosium”. Bachelor thesis. University Heidelberg, 2022.
- [37] Britta Bader. “Absorption Imaging for Ultracold Gases of Dysprosium: Optical Set-Up, Noise Analysis and Investigation of the Fitting Routine’s Reliability”. Bachelor thesis. University Heidelberg, 2023.
- [38] Valentina Salazar Silva. “The Accordion Lattice: Towards Trapping of Dysprosium Ultracold Gases in Two Dimensions”. Master Thesis. University Heidelberg, 2023.
- [39] Charles Drevon. “Characterisation of an accordion lattice setup for a low-dimensional dipolar quantum gases experiment”. Internship report. University Heidelberg, 2023.
- [40] Thibault Bourgeois. “Tailorable optical trap with Digital Micromirror Device for Dysprosium experiment”. M2 report. University Heidelberg, 2023.
- [41] Tadas Pyragius. “Developing and building an absorption imaging system for Ultracold Atoms”. In: *arXiv preprint arXiv:1209.3408* (2012).
- [42] Matthias Wenzel. “A dysprosium quantum gas in highly controllable optical traps”. Master Thesis. University Stuttgart, 2015.
- [43] Maurus Hans. “Physical Computing on a Versatile Setup for Ultra-cold Potassium”. PhD Thesis. Heidelberg University, 2022.
- [44] Klaus Hueck, Niclas Luick, Lennart Sobirey, Jonas Siegl, Thomas Lompe, Henning Moritz, Logan W. Clark, and Cheng Chin. “Calibrating high intensity absorption imaging of ultracold atoms”. In: *Opt. Express* 25.8 (Apr. 2017), pp. 8670–8679. DOI: 10.1364/OE.25.008670.
- [45] Tobias Fabian Schmidutz. “Studies of a Homogeneous Bose Gas”. PhD Tesis. University of Cambridge, 2014.

-
- [46] Bahaa EA Saleh and Malvin Carl Teich. *Fundamentals of photonics*. John Wiley & sons, 2019.
- [47] Eugene Hecht. *Optics*. Pearson Education India, 2012.
- [48] Thomas Öttl. “Designing and testing an objective for imaging ultracold quantum gases”. Master Thesis. University of Innsbruck, 2019.
- [49] Vasudevan Lakshminarayanan and Andre Fleck. “Zernike polynomials: a guide”. In: *Journal of Modern Optics* 58.7 (2011), pp. 545–561. DOI: 10.1080/09500340.2011.554896.
- [50] Max Born and Emil Wolf. *Principles of optics: electromagnetic theory of propagation, interference and diffraction of light*. Elsevier, 2013.
- [51] Kuo Niu and Chao Tian. “Zernike polynomials and their applications”. In: *Journal of Optics* 24.12 (2022), p. 123001.
- [52] Micha Bunjes. “High-Resolution Optics for Modular Quantum Simulation”. Master Thesis. University of Heidelberg, 2022.
- [53] Michael W Davidson and Mortimer Abramowitz. “Optical microscopy”. In: *Encyclopedia of imaging science and technology* 2.1106-1141 (2002), p. 120. DOI: 10.1002/0471443395.img074.
- [54] Maurice Rieger. “Magnetic field characterisation and spin manipulation in ultracold dysprosium using radio-frequency driving and AC Stark shifts”. Bachelor thesis. University Heidelberg, 2023.
- [55] C.E. Shannon. “Communication in the Presence of Noise”. In: *Proceedings of the IRE* 37.1 (1949), pp. 10–21. DOI: 10.1109/JRPROC.1949.232969.

List of Figures

2.1	Energy level diagram of dysprosium	6
2.2	Experimental overview	8
2.3	Level scheme 421 nm transition in dysprosium	11
3.1	The 4f-system	15
3.2	The Airy Disk pattern	17
3.3	Aberrated and ideal wavefront	20
3.4	the Zernike circle polynomials	21
3.5	Structure of the Simulations	22
3.6	Simulated Cross Section	23
3.7	Diffraction from a slit	24
4.1	Microscope objective housing and position	26
4.2	Focus and backfocus of the objective	29
4.3	Chromatic focal shift of the microscope objective	32
4.4	Coating curves of the microscope objective	33
5.1	Scheme of the experimental test setup	37
5.2	Breadboard of the test setup	38
5.3	Camera view during alignment	39
5.4	Commercial Objective Measurement Plots	42
5.5	Back focus test setup	44
5.6	Backfocus Measurement	45
5.7	Resolution Measurement Results	46
5.8	Depth of field Measurement Results	48
5.9	Field of View Measurement Results	50
5.10	Tilt Measurements Results	51
5.11	Dichroic mirror in its mount	53
5.12	Measurements with Dichroic mirror	54
6.1	Microscope objective final assembly	57

List of Tables

2.1	Abundances of dysprosium isotopes	5
4.1	PSF radius and depth of field	30
4.2	Expected transmission coefficients	33
5.1	Commercial Objective Measurement Results	42
5.2	Measurement results for PSF radius and Depth of Field	47
5.3	Measurement results for the Field of View	49
5.4	Measured transmission coefficients	52

Acknowledgements

First and foremost, I want to thank Lauriane Chomaz for the opportunity to be a part of the Quantum fluids group and work on the dysprosium experiment. Her guidance and support during the supervision of my Master thesis were invaluable, and I received the best mentorship I could have hoped for.

Additionally, I want to thank Selim Jochim for being the second corrector of my thesis.

Big thanks go to the whole Quantum Fluids group! Thank you, Karthik Chandrashekhara, Jianshun Gao, and Shuwei Jin for answering all my questions, Charles Drevon and Thibault Bourgeois for the French lessons (and your patience), Wyatt Kirky for the tea times, as well as Britta Bader, Christian Gölzhäuser, Nele Griesbach, Jonah Lux, Joschka Schöner, Maurice Rieger, and Valentina Salazar Silva for all the lunch breaks, discussions, and group activities.

Thanks also to Micha Bunjes, Tobias Hammel, and Maximilian Kaiser from the HQA group, who borrowed me equipment for the test setup and helped out with plenty of questions in the beginning.

Additionally, thanks to Andreas Düll and the other people from the workshop for having the patience to understand my drawings and produce the parts for my setup.

I want to say thank you to all my study friends for helping me to manage this time by providing a lot of moral support, reading my thesis for correction, and playing card games.

Finally, I want to thank my family and my boyfriend, Marcel, for the unconditional love and support they provide me all the time ♡

Erklärung

Ich versichere, dass ich diese Arbeit selbstständig verfasst habe und keine anderen als die angegebenen Quellen und Hilfsmittel benutzt habe.

Heidelberg, den 14.12.2023

Sarah Philips

S. Philips